Proceedings of the Project Review, Geo-Mathematical Imaging Group (Purdue University, West Lafayette IN), Vol. 1 (2013) pp. 75-102.

A DISCONTINUOUS GALERKIN METHOD FOR MODELING MARINE CONTROLLED SOURCE ELECTROMAGNETIC DATA

TORGEIR WIIK*, MAARTEN V. DE HOOP†, AND BJøRN URSIN‡

Abstract. We present a discontinuous Galerkin (DG) method for the time harmonic, diffusive Maxwell's equations, with a view towards modeling marine Controlled Source Electromagnetic (mCSEM) data for geophysical exploration. We treat the first order Maxwell system, which gives us the same approximation order in both the electric and magnetic fields, and ensures that we do not need the penalty term used when treating the second order double-curl formulation. Due to the discontinuous approximation space, the DG method accomodates large parameter contrasts, and it is flexible with respect to both local mesh and polynomial order refinements. These properties make the method suited for mCSEM modeling. In the implementation we allow a completely unstructured mesh, and utilize a centered flux and a first order approximation space. For this setting we estimate a first order convergence rate. We further demonstrate the method in the so-called 2.5D setting to model mCSEM data, and show the accuracy of the method in models in which highly accurate numerical solutions can be obtained using alternative methods. Finally, we demonstrate the method on more realistic examples and illustrate the physics of mCSEM.

Keywords: Controlled source electromagnetic, discontinuous Galerkin method

1. Introduction. In this paper we consider a discontinuous Galerkin method for solving the time harmonic, diffusive Maxwell's equations. The framework is formulated in context of marine Controlled Source Electromagnetics (mCSEM) for hydrocarbon prospecting, but is completely general. In mCSEM, low-frequency, electromagnetic signals are used for hydrocarbon prospecting, and it is a relatively new achievement; the first Seabed Logging (SBL) survey was conducted by Statoil offshore Angola in 2000 [14]. Marine Controlled Source Electromagnetic (mCSEM) surveys are usually performed by towing a horizontal, electric dipole which outputs a binary waveform, thus generating electromagnetic signals, behind a vessel. Usually the signal's frequencies lie in the range $0.1\text{Hz} - 10\text{Hz}$, as these frequencies penetrate into the relevant depths of the subsurface. Receivers that measure the electric and magnetic field are placed on the seabed (See Figure 1). The electromagnetic properties of a medium are described by its electric permittivity, electric conductivity and magnetic permeability. A hydrocarbon reservoir will typically possess a lower electric conductivity compared to its surroundings, which means that the electromagnetic signals from the dipole will scatter when they hit the reservoir. From measuring this scattered field at the receivers we can be able to predict the location of a possible reservoir, and what kind of fluid (oil, gas, water) it contains. Modeling this scattered response in known models constitutes the forward scattering problem, which we will consider in this paper. Due to the conductive media and low, distinct frequencies, the governing equations are the time harmonic diffusive Maxwell's equations, i.e. Maxwell's equations including conduction currents.

To model the response of a mCSEM experiment we apply the discontinuous Galerkin (DG) method, see [16] for an introduction. [16] describes very well the development of the DG method for time dependent problems and how it relates to the finite volume (FV) method. The DG method can be viewed as a mixture between conventional finite element methods and FV methods; over each element in the mesh the solution is expanded in a chosen basis, and to connect this element to its neighbors in a consistent way a numerical flux is specified along the element boundaries. Although the FV method allows an unstructured mesh, the introduction of higher order spatial approximations extends the stencil to several elements in the mesh, not only neighbors. This is one important difference between FV and DG methods; increasing the spatial approximation order in the DG method still preserves the local formulation as every basis function has support over a single element only. This leads to a method which is very flexible with respect to the computational mesh.

*Department for Petroleum Engineering and Applied Geophysics, The Norwegian University of Science and Technology, S.P. Andersensvei 15A, 7491 Trondheim, Norway. Presently: Statoil Research Center, Arkitekt Ebbelsveg 10, 7053 Ranheim, Norway.

†Department of Mathematics, Purdue University, 150 N. University Street, West Lafayette, IN 47907, USA.

‡Department for Petroleum Engineering and Applied Geophysics, The Norwegian University of Science and Technology, S.P. Andersensvei 15A, 7491 Trondheim, Norway.

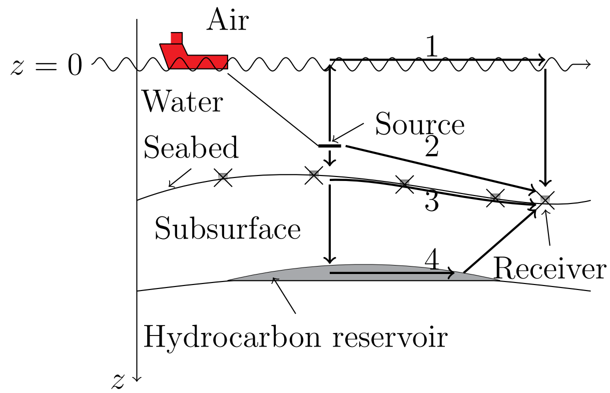

Fig. 1. *Figure displaying a usual configuration of a mCSEM survey. A horizontal electric dipole is towed behind a vessel, while receivers are placed on the seabed. Main sources for measured response are: 1:Interaction with sea-air interface, 2:direct wave, 3:Response from the seabed, 4:Response from hydrocarbon reservoir. The figure is retrieved from [21].*

Choosing order zero polynomial basis functions in DG will recover a FV method. For an example of a FV method for the time domain Maxwell's equations related to our formulation, see [27].

Finite element methods for solving Maxwell's equations in the mCSEM context exist in many different forms. In the 2.5D setting, with medium invariance in the strike direction, [32] presented a coupled set of scalar second order equations for the strike components of the electric and magnetic fields. A finite element method was applied to these equations by [18], and has the advantage that the degrees of freedom is reduced and continuous elements may be used. However, to obtain the most frequently used field component, the inline electric field, it requires a differentiation of the solution, and the implementation of anisotropy is less straightforward compared to using the first order system. To honor the discontinuous nature of the electromagnetic fields at material interfaces it is common to use curl-conforming elements [26] for 3D finite element methods. These ensure that the proper discontinuities are allowed at interfaces between tetrahedrons in the mesh. This path was taken by for instance [11], and applied to a second order equation for the electric field. This implies that a differentiation is needed to obtain magnetic field components. In this paper, we investigate how a fully discontinuous method, namely DG, applied to the mCSEM problem through the complete first order Maxwell system behaves.

The DG method was first applied to hyperbolic PDEs in 1973 to model neutron transport [28], and subsequently a theoretical analysis of DG methods followed, see for instance [17]. More recently, the interest in DG methods has increased and many contributions to theory and applications have been made during the last two decades. Confer to [8] for a summary of the development of DG methods until 2000.

The DG method for elliptic problems originates from finite element methods using interior penalties (IP) to weakly enforce continuity conditions between elements, see for instance [2, 3, 13, 4, 35, 1]. The interior penalty methods arose around the same time as the DG method for hyperbolic equations. We use a formulation based on the first order system of equations, an approach which is similar to the method used by [12], and also closely related to the work in [15]. We note that the solution of Maxwell's equations in the frequency domain using DG methods has also been studied in the context of second order *curl-curl* equations using IP methods, see for instance [30] and the references therein, and so called local DG methods [10, 6]. The first order system has advantages in as much as that one avoids numerical differentiation to obtain the "second" field (in the *curl-curl* formulation you solve for either the electric or magnetic field), as both the electric and magnetic field are observed in mCSEM. However, we have to solve for twice the number of field components. The motivation for applying the DG method to this problem lies in the treatment of discontinuities in the electromagnetic fields at material interfaces, i.e. geological interfaces, in the subsurface. Further, the DG method is flexible with respect to the computational mesh, which should prove an advantage for the discretization geophysical models. For instance, conventional finite difference methods usually require a regular mesh, and may have problems at interfaces with large material contrasts. The DG method handles this naturally, and the method is implemented for completely unstructured meshes.

We present a DG method for the mCSEM problem using unstructured meshes and linear basis functions to accomodate the slowly varying fields in homogeneous regions and the limited regularity of the PDE coefficients, but the DG method is also flexible with respect to local polynomial order refinements. The choice of first order basis functions was also made with a view towards simplicity for non-specialist users of the code. The problem is formulated as a first order system, thus avoiding the penalty terms which are introduced in the *curl-curl* formulation. A Perfectly Matched Layer is implemented to simulate the radiation condition on the finite computational domain. This formulation using the DG method admits large jumps in the conductivity. This is essential for the mCSEM problem where the conductivity varies over many orders of magnitude. First, we perform some numerical tests using 1D Maxwell's equations, to investigate if it is worthwhile to proceed to realistic problems. Finally, we consider the so called 2.5D setting, with model invariance along one direction. We validate the implementation using a plane layer model, for wich very accurate solutions exist. After this we consider two realistic examples in the 2.5D setting to demonstrate and explain the physics behind mCSEM prospecting. The error of the scheme is estimated to decay linearly as a function of mesh size.

2. Basic equations.

2.1. Problem formulation. Let σ, ϵ and μ denote the electric conductivity, electric permittivity and magnetic permeability, which are assumed to be real, non-negative L^∞ functions. We further accept the constitutive relations $\mathbf{d} = \epsilon\mathbf{e}$, $\mathbf{b} = \mu\mathbf{h}$ and $\mathbf{j}^c = \sigma\mathbf{e}$, where $\mathbf{d}, \mathbf{e}, \mathbf{b}, \mathbf{h}$ denote the electric displacement field, electric field, magnetic flux density and magnetic field strength, respectively, and $\mathbf{j}^c$ denotes the conduction current set up by an imposed electric field. These vectors take on values in $\mathbb{C}^3$. This leads us to the following form of Maxwell's time harmonic curl equations in $\mathbb{R}^3$ [33]:

$$\nabla \times \mathbf{e} = \mathrm{i}\omega\mu_0\mathbf{h}, \tag{2.1}$$

$$\nabla \times \mathbf{h} = \tilde{\sigma}\mathbf{e} + \mathbf{j}^s, \tag{2.2}$$

where $\mathrm{i} = \sqrt{-1}$, $\omega = 2\pi f$, $\tilde{\sigma} = \sigma - \mathrm{i}\omega\epsilon$ and $\mathbf{j}^s$ is the source current density. Here f denotes the frequency and μ_0 is the freespace permeability. We allow σ to be a rank 2 tensor, where $\sigma_{11} = \sigma_{22} = \sigma_h$, $\sigma_{33} = \sigma_v$ and $\sigma_{ij} = 0, i \neq j$. This is known as TIV anisotropy (transversally isotropic in the vertical direction), and allows for different conductivities in the horizontal and vertical directions. This is a useful case for geophysical applications as the subsurface is often stratified, and thus causes this anisotropy.

The source $\mathbf{j}^s$ is a horizontal electric dipole for mCSEM applications, with polarization given by $l = [l_x, l_y, 0]^T$, where $|l|$ is the length of the source, and current amplitude $I(\omega)$. The source dipole moment is given by $I\,|l|$. This is well approximated by a point dipole, $Il\delta(\mathbf{x} - \mathbf{x}_s)$, when $|l| \ll |\mathbf{x} - \mathbf{x}_s|$, where $\mathbf{x}_s$ is the source position [21]. Numerically we will use an approximation to a point source such that $\mathbf{j}^s \in \left[L^2\left(\mathbb{R}^3\right)\right]^3$, which is needed in the later weak formulation. The source function is explicitly given later.

In our applications the frequencies lie in the range $0.1-10$Hz. In the watercolumn and sediments we have $\tilde{\sigma} \approx \sigma$, i.e. the quasi-static approximation [25] applies, which means that the equations describe a diffusion process instead of wave propagation. This is because of the low frequencies, the fact that the conductivity of sea-water is approximately 3.2S/m (around 1S/m for water filled sediments) and the permittivity is usually of the same order as the freespace permittivity, $\epsilon = \epsilon_0 = 8.85 \cdot 10^{-12}$F/m.

Further, we assume that the fields decay as they propagate towards infinity, which is expressed through the Silver-Müller radiation condition. This is expressed as [19]

$$\begin{aligned}\left|\sqrt{\tilde{\epsilon}}\mathbf{e} - \mathbf{h} \times \frac{\mathbf{r}}{r}\right| &\leq \frac{c}{r^2},\\ |\mathbf{e}| &\leq \frac{c}{r},\\ |\mathbf{h}| &\leq \frac{c}{r},\end{aligned} \tag{2.3}$$

for large r. Here $\tilde{\epsilon} = \epsilon + \mathrm{i}\frac{\sigma}{\omega}$, $\mathbf{r} = \mathbf{x} - \mathbf{x}_s$, $r = |\mathbf{r}|$ and c is a generic constant.

We consider solving equations 2.1 and 2.2 on a bounded domain $\Omega \subset \mathbb{R}^3$ with appropriate boundary conditions imposed on $\partial\Omega$. These boundary conditions will be specified later, and will correspond to those introduced for the Perfectly Matched Layers (PML) as discussed in Appendix A. We introduce the Sobolev space

$$W = H(\mathrm{curl};\Omega) = \left\{f \in \left[L^2(\Omega)\right]^3 : \nabla \times f \in \left[L^2(\Omega)\right]^3\right\},$$

and assume $\mathbf{j}^s \in \left[L^2(\Omega)\right]^3$. W is the natural space for Maxwell's equations. We further denote the standard L^2 inner product over Ω by

$$(a,b)_\Omega = \int_\Omega a \cdot \bar{b}\,\mathrm{d}\mathbf{x},$$

where the overline denotes complex conjugate. We proceed by multiplying equations 2.1 and 2.2 with $v \in \mathcal{D}$, where $\mathcal{D}$ is a space of sufficiently smooth test functions, and integrating the result over Ω:

$$(\nabla \times \mathbf{e}, v)_\Omega = \mathrm{i}\omega\mu_0 (\mathbf{h}, v)_\Omega, \tag{2.4}$$

$$(\nabla \times \mathbf{h}, v)_\Omega = (\tilde{\sigma}\mathbf{e}, v)_\Omega + (\mathbf{j}^s, v)_\Omega. \tag{2.5}$$

Performing integration by parts then yields

$$\int_{\partial\Omega} \overline{v} \cdot (\mathbf{n} \times \mathbf{h})\,\mathrm{d}S + (\mathbf{h}, \nabla \times v)_\Omega = (\tilde{\sigma}\mathbf{e}, v)_\Omega + (\mathbf{j}^s, v)_\Omega, \tag{2.6}$$

$$\int_{\partial\Omega} \overline{v} \cdot (\mathbf{n} \times \mathbf{e})\,\mathrm{d}S + (\mathbf{e}, \nabla \times v)_\Omega = \mathrm{i}\omega\mu_0 (\mathbf{h}, v)_\Omega, \tag{2.7}$$

where $\mathbf{n}$ is the outward pointing unit normal, and $\mathrm{d}S$ is a surface measure. This yields the following weak formulation of our problem:

Find $\mathbf{e}, \mathbf{h} \in W$ such that equations 2.6 and 2.7 holds $\forall v \in \mathcal{D}$.

The measurements $\mathbf{e}_{\mathrm{meas}}, \mathbf{h}_{\mathrm{meas}}$, taken along a line or on a surface $\mathcal{S}$, are then expressed as the restriction of $\mathbf{e}$ and $\mathbf{h}$ to $\mathcal{S}$. That is,

$$\mathbf{e}_{\mathrm{meas}} = \mathbf{e}\mid_{\mathcal{S}}, \mathbf{h}_{\mathrm{meas}} = \mathbf{h}\mid_{\mathcal{S}}.$$

All field components are usually measured, with the exception of the vertical electric field. Engineering challenges prevent this from being measured accurately.

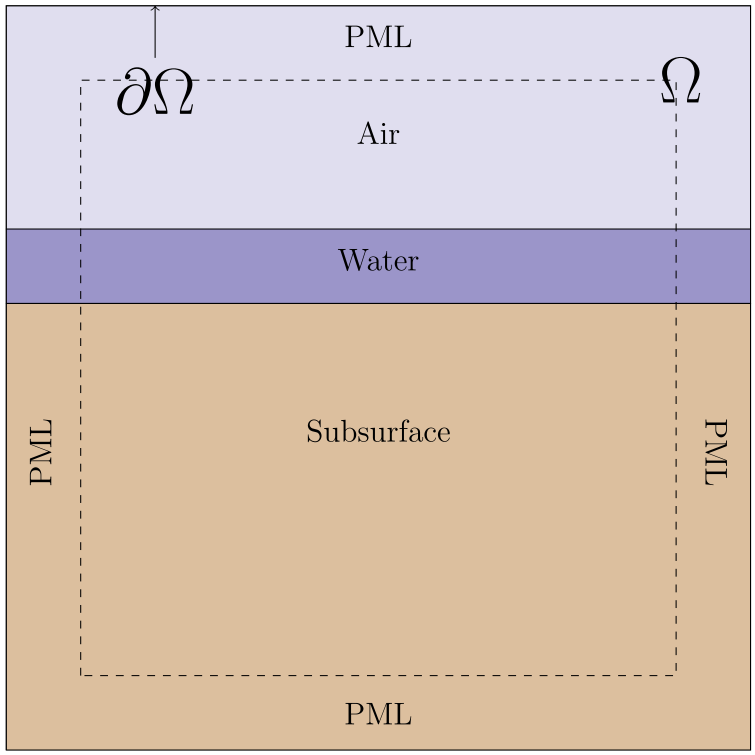

Fig. 2. *Intersection of domain* Ω.

3. The Discontinuous Galerkin Method.

3.1. Mesh and approximation space. We solve equations 2.6 and 2.7 numerically for $\mathbf{e}$ and $\mathbf{h}$ using the DG method on a bounded domain $\Omega \subset \mathbb{R}^3$, where $\mathbf{n} \times \mathbf{e} = 0$ is imposed on $\partial\Omega$. Inside $\partial\Omega$ a PML zone, where the fields are attenuated without causing any reflection back into the model, is incorporated to simulate the radiation condition, as shown in Figure 2. Further, we consider a non-zero electric permittivity ϵ, which means that we do not consider the quasi static approximation which is often used in this setting [25]. It is assumed that the air layer is chosen thick enough to account for the interaction between the water column and the air.

We consider $\Omega_h, h > 0$, to be a family of discretized approximations to Ω such that $\overline{\Omega}_h = \bigcup_{K \in \tau_h} \overline{K}$, where τ_h is a tesselation of Ω_h into N_K simplices K, i.e. tetrahedrons in 3D. We denote the set of facets by Γ, facets between two neighboring elements by Γ^i, and the facets on $\partial\Omega_h$ as Γ^b. Naturally, $\Gamma = \Gamma^i \cup \Gamma^b$ and $\Gamma^i \cap \Gamma^b = \emptyset$.

We consider aproximate solutions $\left(\mathbf{e}^h, \mathbf{h}^h\right) \in X \times X$, where

$$X = \left\{ f \in \left[L^2\left(\Omega_h\right)\right]^3 : \forall K \in \tau_h, f\mid_K \in \left[\mathcal{P}^1\left(K\right)\right]^3 \right\}.$$

Here $\mathcal{P}^1\left(K\right)$ is the space of polynomials of at most degree 1 over K. Since we consider a Galerkin type method, the space of test functions is chosen equal to the solution space.

3.2. Local weak formulation. We obtain the local weak formulation for the discrete solution by considering the weak formulation over a single element $K \in \tau_h$:

$$\int_{\partial K} v \cdot (\mathbf{n} \times \mathbf{h}^*)\,\mathrm{d}S + \left(\mathbf{h}^h, \nabla \times v\right)_K = \left(\tilde{\sigma}\mathbf{e}^h, v\right)_K + (\mathbf{j}^s, v)_K\,, \tag{3.1}$$

$$\int_{\partial K} v \cdot (\mathbf{n} \times \mathbf{e}^*)\,\mathrm{d}S + \left(\mathbf{e}^h, \nabla \times v\right)_K = \mathrm{i}\omega\mu_0 \left(\mathbf{h}^h, v\right)_K\,, \tag{3.2}$$

where $\mathbf{e}^*, \mathbf{h}^*$ are the numerical fluxes which remain to be specified, and $v \in X$. As the basis for X is chosen as real valued functions, and it suffices to consider the basis functions, the complex conjugate in the weak formulation is omitted. This yields the following local discrete weak formulation of our problem:

Find $\mathbf{e}^h, \mathbf{h}^h \in X$ such that equations 3.1 and 3.2 hold $\forall v \in X$, for each $K \in \tau_h$.

To couple each element to its neighbours and to ensure consistency a numerical flux needs to be specified at the element boundaries, as the fields take on two values at each internal facet due to the discontinuities. Several choices for specifying the flux term have been explored, for instance the upwinding flux [12] is popular for flow problems. We choose to use the centered flux [12], as for the diffusion dominated problem there is no wave motion as such. We thus use

$$\mathbf{e}^* = \{\{\mathbf{e}\}\} = \frac{1}{2}\left(\mathbf{e}^{h,+} + \mathbf{e}^{h,-}\right),$$

and similarly for the magnetic field. Here $+/-$ denotes each side of the boundary surface. For each tetrahedral element K we may write $\partial K = \bigcup_{k=1}^{4} F_k$, where F_k is a facet of the tetrahedron, and over each such facet the normal vector is constant. Since the pairwise intersection of facets on a given tetrahedron has zero surface measure we may write the integral as the sum of the integrals over each face. At the boundary $\partial\Omega_h$, where there are no neighbours, we implement the boundary condition $\mathbf{n} \times \mathbf{e} = 0$, and define $\mathbf{h}^* = \{\{\mathbf{h}\}\} = \mathbf{h}^{h,+}$, i.e. the limit of the value in the element. This may cause reflection at the boundary, but will nevertheless be attenuated by the PML zone.

3.3. Global weak formulation. The global weak formulation is obtained by summing equations 3.1 and 3.2 over the elements, thus obtaining

$$\begin{aligned}\sum_{F \in \Gamma^i} \int_F [[v]] \cdot (\mathbf{n} \times \{\{\mathbf{h}\}\})\,\mathrm{d}S + \sum_{F \in \Gamma^b} \int_F v \cdot (\mathbf{n} \times \{\{\mathbf{h}\}\})\,\mathrm{d}S \\ + \sum_{K \in \tau_h} \left(\mathbf{h}^h, \nabla \times v\right)_K = \left(\tilde{\sigma}\mathbf{e}^h, v\right)_{\Omega_h} + (\mathbf{j}^s, v)_{\Omega_h}\,,\end{aligned} \tag{3.3}$$

$$\sum_{F \in \Gamma^i} \int_F [[v]] \cdot (\mathbf{n} \times \{\{\mathbf{e}\}\})\,\mathrm{d}S + \sum_{K \in \tau_h} \left(\mathbf{e}^h, \nabla \times v\right)_K = \mathrm{i}\omega\mu_0 \left(\mathbf{h}^h, v\right)_{\Omega_h}\,, \tag{3.4}$$

where $[[v]]$ is the *jump* of v across the inter-element interface, as defined in [12]. This yields the following global discrete weak formulation of our problem:

Find $\mathbf{e}^h, \mathbf{h}^h \in X$ such that equations 3.3 and 3.4 holds $\forall v \in X$.

3.4. Boundary and interface operators. At this point it is straightforward to make the connection to the boundary operator M_F for $F \in \Gamma^b$, and the interface operator D_F for $F \in \Gamma^i \cup \Gamma^b$, as presented in [15]. To do this we first separate the source term and write

$$
\begin{aligned}
&\left(\tilde{\sigma}\mathbf{e}^h, v\right)_{\Omega_h} - \sum_{F\in\Gamma^i}\int_F [[v]]\cdot(\mathbf{n}\times\{\{\mathbf{h}\}\})\,\mathrm{d}S - \sum_{F\in\Gamma^b}\int_F v\cdot(\mathbf{n}\times\{\{\mathbf{h}\}\})\,\mathrm{d}S \\
&\qquad - \sum_{K\in\tau_h}\left(\mathbf{h}^h, \nabla\times v\right)_K = -\left(\mathbf{j}^s, v\right)_{\Omega_h}, \qquad (3.5)
\end{aligned}
$$

$$
\mathrm{i}\omega\mu_0\left(\mathbf{h}^h, v\right)_{\Omega_h} - \sum_{F\in\Gamma^i}\int_F [[v]]\cdot(\mathbf{n}\times\{\{\mathbf{e}\}\})\,\mathrm{d}S - \sum_{K\in\tau_h}\left(\mathbf{e}^h, \nabla\times v\right)_K = 0. \qquad (3.6)
$$

We rewrite this as a single equation for $\mathbf{w}^h = \left(\mathbf{e}^h, \mathbf{h}^h\right) \in X\times X$ as

$$
\begin{aligned}
&\int_{\Omega_h} G_0\mathbf{w}^h\cdot\tilde{v}\mathrm{d}\mathbf{x} - \sum_{F\in\Gamma^i}\int_F [[\tilde{v}]]\cdot G_{\mathbf{n}}\{\{\mathbf{w}\}\}\,\mathrm{d}S - \sum_{F\in\Gamma^b}\int_F \tilde{v}\cdot G_{\mathbf{n}}\{\{\mathbf{w}\}\}\,\mathrm{d}S \\
&\qquad - \sum_{K\in\tau_h}\int_K \mathbf{w}^h\cdot\sum_{l=x,y,z} G_{\mathbf{e}_l}\frac{\partial}{\partial l}\tilde{v}\mathrm{d}\mathbf{x} = -\int_{\Omega_h}\mathbf{j}\cdot\tilde{v}\mathrm{d}\mathbf{x}, \qquad (3.7)
\end{aligned}
$$

where $\tilde{v}\in X\times X$ and $\mathbf{j} = \left[\mathbf{j}^s, 0_{1\times 3}\right]^T$, and

$$
G_0 = \begin{pmatrix} \tilde{\sigma}I_{3\times 3} & 0_{3\times 3} \\ 0_{3\times 3} & \mathrm{i}\omega\mu_0 I_{3\times 3}\end{pmatrix}, G_{\mathbf{n}} = \begin{pmatrix} 0 & N \\ N & 0\end{pmatrix}, N = \begin{pmatrix} 0 & -n_z & n_y \\ n_z & 0 & -n_x \\ -n_y & n_x & 0\end{pmatrix}.
$$

Here $\mathbf{e}_l$ is the canonical basis for $\mathbb{R}^3$. Following [15] we assume that M_F and D_F are associated with matrix valued fields, $\mathcal{M}_F : \Gamma^b \to \mathbb{R}^{6,6}$ and $\mathcal{D}_F : \Gamma^b\cup\Gamma^i \to \mathbb{R}^{6,6}$, respectively. We find that

$$
\mathcal{D}_F = -G_{\mathbf{n}}, \qquad (3.8)
$$

$$
\mathcal{M}_F = -\tilde{G}_{\mathbf{n}}, \qquad (3.9)
$$

with

$$
\tilde{G}_{\mathbf{n}} = \begin{pmatrix} 0 & N \\ -N & 0\end{pmatrix}.
$$

This specifies the actions of the operators on a vector through the matrix-vector product. It is evident that multiplication with N corresponds to the cross product with $\mathbf{n}$, and the construction of $G_{\mathbf{n}}, \tilde{G}_{\mathbf{n}}$ ensures that $\mathbf{n}\times\mathbf{e}$ vanishes on the boundary.

It may be verified that our system does not fit into the Friedrichs's systems framework treated by [15] because of the fact that the coefficients are complex, nor does the central flux satisfy the conditions set in [15] on boundary and interface operators for convergence. We note that on $F\in\Gamma^i$, $\mathcal{D}_F$ is double valued, although its mean is zero, while on Γ^b, $\mathcal{D}_F$ is single valued.

4. Discretization.

4.1. 3D Source representation. Due to the restriction to a space of first order polynomials we choose to implement the source as a normalized cone over $\mathbb{R}^3$:

$$
\mathbf{j}^s = \begin{cases} \frac{3}{\pi\tau^4}(\tau - r)\,\hat{\mathbf{d}}, & r\le\tau \\ 0, & otherwise\end{cases},
$$

where $r^2 = (x-x_s)^2 + (y-y_s)^2 + (z-z_s)^2$ is the squared euclidian distance to the source, and $\hat{\mathbf{d}} = [\cos\alpha, \sin\alpha, 0]^T$ describes the source polarization, where α is the angle between the source polarization and the x-axis in the horizontal plane. This choice is made as we model a horizontal electric dipole. This source has a unit dipole moment.

4.2. Discrete system. In this section we describe the linear system of equations using linear basis functions. The corresponding system with higher order basis functions (p-refinement) can be deduced by following the same procedure. It is easily verified that

$$\Big\{[1,0,0]^T, [0,1,0]^T, [0,0,1]^T, [x',0,0]^T, [y',0,0]^T, [z',0,0]^T,$$
$$[0,x',0]^T, [0,y',0]^T, [0,z',0]^T, [0,0,x']^T, [0,0,y']^T, [0,0,z']^T\Big\}$$
$$= \left\{v_K^i : i = 1\dots 12\right\} = X_K$$

is a basis for X restricted to a given element K, where $x' = \frac{1}{L}(x - x_0)$, x_0 is a vertex of the tetrahedron, and L is a characteristic lenght scale of the element. This choice is made to ensure that the expansion coefficients of the solutions in this basis have little dependency on the actual spatial positions of the elements, which should yield a better conditioned system to solve. This is called a modal basis, and differs from the nodal approach as described in [16] where basis functions are constructed around specific points within each element. The basis functions for X are chosen to have support over only one element in the mesh, where they are given as in the definition of X_K. To this end we introduce $\phi_{i;j}$ such that $X = span\{\phi_{i;j} : i = 1\dots 12, j = 1\dots N_K\}$. Specifically, we choose for a given $j = j_0$,

$$\phi_{i;j_0}(\mathbf{x}) = \begin{cases} v^i_{K_{j_0}}(\mathbf{x}), & \mathbf{x} \in K_{j_0} \\ 0, & otherwise \end{cases},$$

where we have introduced an ordering of the elements.

Over a given element K_{j_0} we expand $\mathbf{e}^h$ and $\mathbf{h}^h$ in the chosen basis, i.e. we write $\mathbf{e}^h\,|_{K_{j_0}} = a^1_{e,K_{j_0}}\phi_{1;j_0} + \dots + a^{12}_{e,K_{j_0}}\phi_{12;j_0}$ and $\mathbf{h}^h\,|_{K_{j_0}} = a^1_{h,K_{j_0}}\phi_{1;j_0} + \dots + a^{12}_{h,K_{j_0}}\phi_{12;j_0}$, where $a^i_{e/h,K_{j_0}} \in \mathbb{C}, i = 1\dots 12$. We insert these representations into equations 3.3 and 3.4, which yields 24 equations to determine the 24 unknown expansion coefficients over K_{j_0}, coupled to the expansion coefficients of the neighbouring elements through the flux. We note that each integral in the weak formulation can be calculated analytically, with the exception of $\left(\tilde{\sigma}\mathbf{e}^h, v\right)_K$ if $\tilde{\sigma}$ is allowed to vary within the elements, and perhaps the source integral depending on the source. These integrals are evaluated using a Gaussian quadrature. Quadrature rules over different geometrical shapes, and of different order, can be found in e.g. [34].

We may organize the system of equations as

$$\begin{pmatrix} A & B \\ \tilde{B} & C \end{pmatrix}\begin{pmatrix} E \\ H \end{pmatrix} = \begin{pmatrix} J \\ 0 \end{pmatrix}, \tag{4.1}$$

where $A, B, \tilde{B}, C \in \mathbb{C}^{12N_K \times 12N_K}$, $E, H \in \mathbb{C}^{12N_K}$ contains the unknown expansion coefficients, and $J \in \mathbb{C}^{12N_K}$ contains the terms from the source integral. Specifically,

$$E = \left[a^1_{e,K_1}, \dots, a^{12}_{e,K_1}, a^1_{e,K_2}, \dots, a^{12}_{e,K_{N_K}}\right]^T, \tag{4.2}$$

$$H = \left[a^1_{h,K_1}, \dots, a^{12}_{h,K_1}, a^1_{h,K_2}, \dots, a^{12}_{h,K_{N_K}}\right]^T. \tag{4.3}$$

Disregarding the boundary conditions, which are implemented in the PML-zone, we find for

$i, j = 1 \ldots N_K$ that the matrices are given by the following sub-matrices:

$$(A)_{ij} = \begin{pmatrix} (\tilde{\sigma}_h \phi_{1;i}, \phi_{1;j})_{K_i} & \cdots & (\tilde{\sigma}_v \phi_{1;i}, \phi_{12;j})_{K_i} \\ \vdots & \ddots & \vdots \\ (\tilde{\sigma}_h \phi_{12;i}, \phi_{1;j})_{K_i} & \cdots & (\tilde{\sigma}_v \phi_{12;i}, \phi_{12;j})_{K_i} \end{pmatrix},$$

$$-(B)_{ij} = -\left(\tilde{B}\right)_{ij} = \begin{pmatrix} \frac{1}{2} I^{\partial K_i}_{i,j,1,1} + \delta_{ij} I^{K_i}_{i,j,1,1} & \cdots & \frac{1}{2} I^{\partial K_i}_{i,j,1,12} + \delta_{ij} I^{K_i}_{i,j,1,12} \\ \vdots & \ddots & \vdots \\ \frac{1}{2} I^{\partial K_i}_{i,j,12,1} + \delta_{ij} I^{K_i}_{i,j,12,1} & \cdots & \frac{1}{2} I^{\partial K_i}_{i,j,12,12} + \delta_{ij} I^{K_i}_{i,j,12,12} \end{pmatrix},$$

$$(C)_{ij} = \mathrm{i}\omega\mu_0 \begin{pmatrix} (\phi_{1;i}, \phi_{1;j})_{K_i} & \cdots & (\phi_{1;i}, \phi_{12;j})_{K_i} \\ \vdots & \ddots & \vdots \\ (\phi_{12;i}, \phi_{1;j})_{K_i} & \cdots & (\phi_{12;i}, \phi_{12;j})_{K_i} \end{pmatrix},$$

where

$$I^{\partial K_i}_{i,j,k,l} = \int_{\partial K_i} \phi_{k;i} \cdot (\mathbf{n}_{K_i} \times \phi_{l;j})\, \mathrm{d}S,$$
$$I^{K_i}_{i,j,k,l} = (\nabla \times \phi_{k;i}, \phi_{l;j})_{K_i},$$

$\mathbf{n}_{K_i}$ is the outward unit normal vector for element K_i, and δ_{ij} is Krönecker's delta. We observe that with the given choice of basis for X, both A and C are block diagonal, while B is a sparse matrix with entries along the diagonal and positions corresponding to neighbours. For the source term we find that

$$J = -\left[(\phi_{1;1}, \mathbf{j}^s)_{K_1}, \ldots, (\phi_{12;1}, \mathbf{j}^s)_{K_1}, (\phi_{1;2}, \mathbf{j}^s)_{K_2}, \ldots, (\phi_{12;N_K}, \mathbf{j}^s)_{K_{N_K}}\right]^T.$$

4.3. Solving the linear equation system. To illustrate the conditioning of the system we show the eigenvalues of the system matrix for a 1D problem, explained in Section 5.1. Further, we show the eigenvalues after using two standard preconditioning techniques, a Jacobi preconditioner and an incomplete LU factorization. Figure 3 displays the eigenvalues in the different cases, and we observe the large spread in eigenvalues for the original matrix. We find that both preconditioning approaches reduce the condition number of the system matrix, but the LU factorization is superior in this case, clustering the eigenvalues around the line $\Re(\lambda) = 1$ with $\Im(\lambda) \leq 1$, as shown in Figure 3. The incomplete LU factorization was perfomed with a cutoff at 10^{-3}.

For the situations considered in the numerical examples in this paper, the size of the matrix is within the capabilities of sparse, direct solvers. A direct solver was thus preferred due to the conditioning of the system and the fact that we want to solve for many source positions, i.e. right-hand-sides. The number of unknowns may be reduced slightly by enforcing divergence free basis functions to explicitly incorporate the divergence conditions in Maxwell's equations locally on each element [9]. This was implemented and found not to yield significant improvements, and will not be discussed further.

5. Numerical examples.

5.1. Numerical experiments in 1D. As a demonstration of concept we consider the 1D frequency domain Maxwell's equations; we restrict the propagation to the x-direction, assume that the medium parameters depend only on this coordinate, and align the coordinate system such that $\mathbf{e} = [0, 0, e_z]^T, \mathbf{h} = [0, h_y, 0]^T$. This yields

$$\tilde{\sigma} e_z - \frac{\partial h_y}{\partial x} = -j^s,$$
$$\mathrm{i}\omega\mu_0 h_y + \frac{\partial e_z}{\partial x} = 0.$$

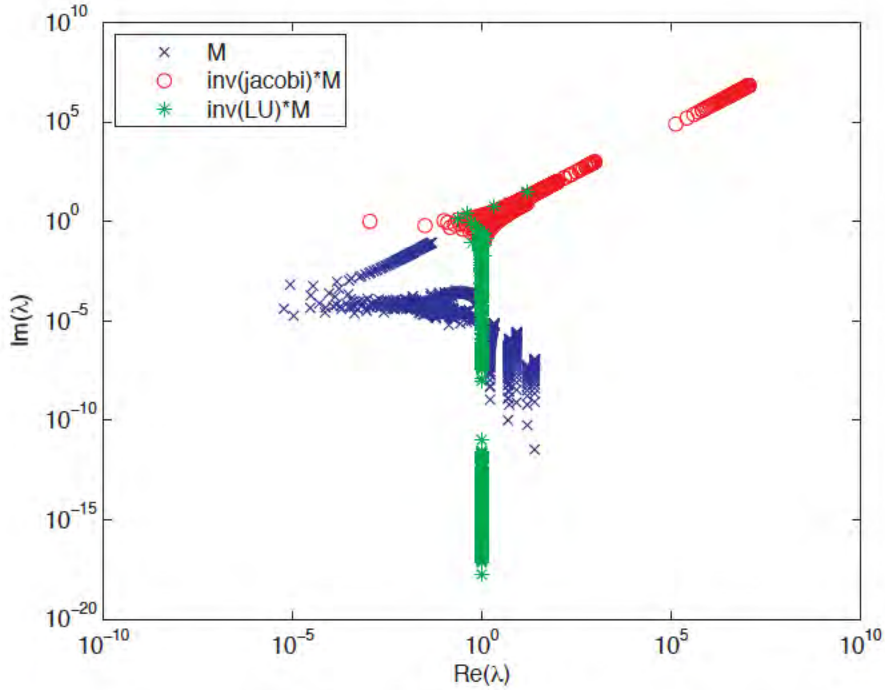

FIG. 3. *Eigenvalues of system matrix under different preconditioners. Blue cross: no preconditioner, red circle: Jacobi preconditioner, green star: incomplete LU preconditioner.*

The source is chosen as a hat function with width κ given by

$$j^s(x) = \begin{cases} \frac{1}{\kappa^2}(x - x_s) + \frac{1}{\kappa}, & x_s - \kappa \le x \le x_s \\ -\frac{1}{\kappa^2}(x - x_s) + \frac{1}{\kappa}, & x_s \le x \le x_s + \kappa \\ 0, & elsewhere \end{cases},$$

where x_s is the center of the source.

5.1.1. Convergence test. First we perform a convergence test. We use a homogeneous $\sigma =$ 1S/m model without any PML zones, $\epsilon = 0$F/m, $\mu = \mu_0$. The source is placed at the center of a 4000m long model with a frequency 1Hz and width of 100m. The solutions obtained for different mesh sizes are compared to a solution with a significantly smaller mesh size to estimate the error. The convergence order is then estimated by comparing the estimated errors at different mesh sizes. We observe from Figure 4 that the convergence appears to be of first order. We note that the PML zones may destroy this convergence rate, especially if the PML parameter χ is chosen large to obtain short PML zones (see Appendix A).

5.1.2. Example with realistic parameters. In this example the source center is set to $x = 350$m, and we consider the typical mCSEM frequency of 0.25Hz. Due to the relatively low computational cost associated with 1D problems we have chosen to use uniform mesh sizes h. The results presented uses 350 intervals, which corresponds to $h = 10$m, including 500m PML zone in each end, and $\kappa = 10$m. Figure 5 displays the profile of the model which is considered ($\mu = \mu_0$).

Figures 6(a) and 6(b) display the magnitude of the calculated magnetic field over the whole model and zoomed in around the source location, respectively. Figure 6(b) shows how well the DG method performs around the difficult source point, and the interface at $x = 400$m, which should make it appropriate for mCSEM modeling.

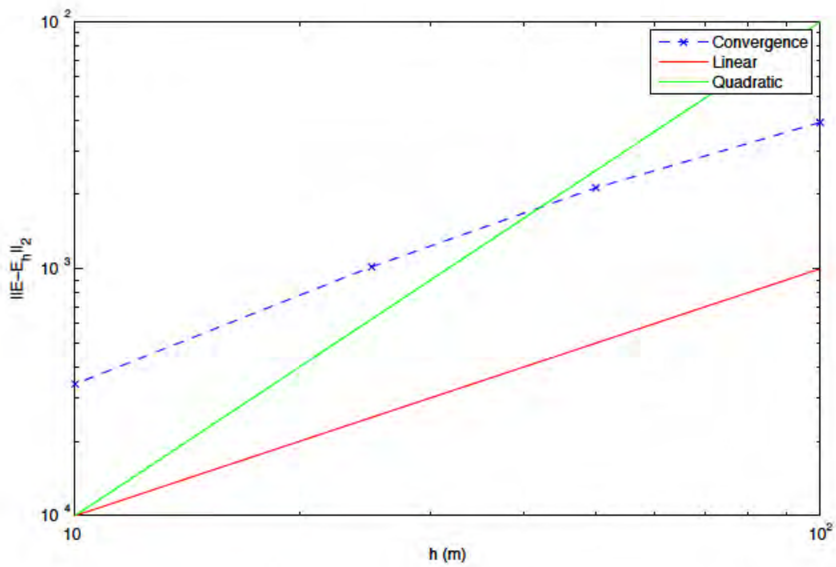

FIG. 4. *1D convergence test. L^2 norm of the error in the electric field against element length (h).*

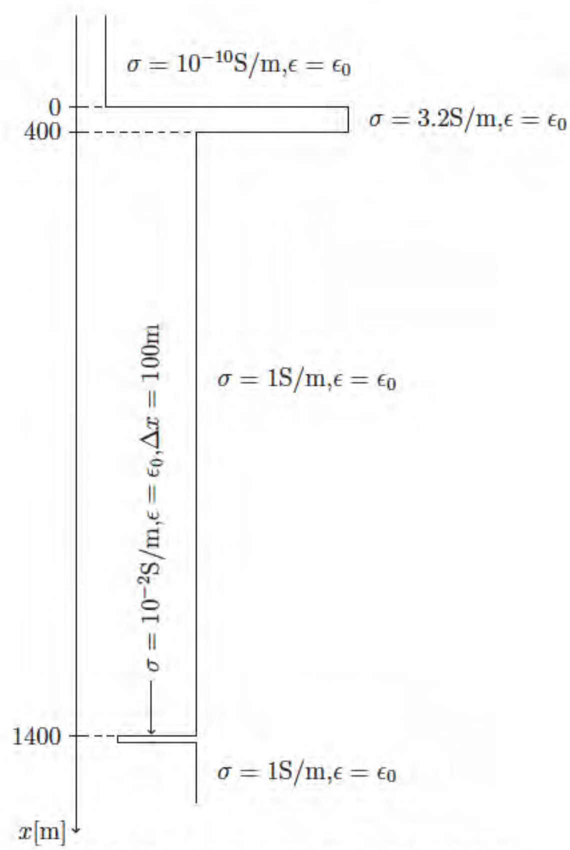

FIG. 5. *Model used in 1D numerical example.*

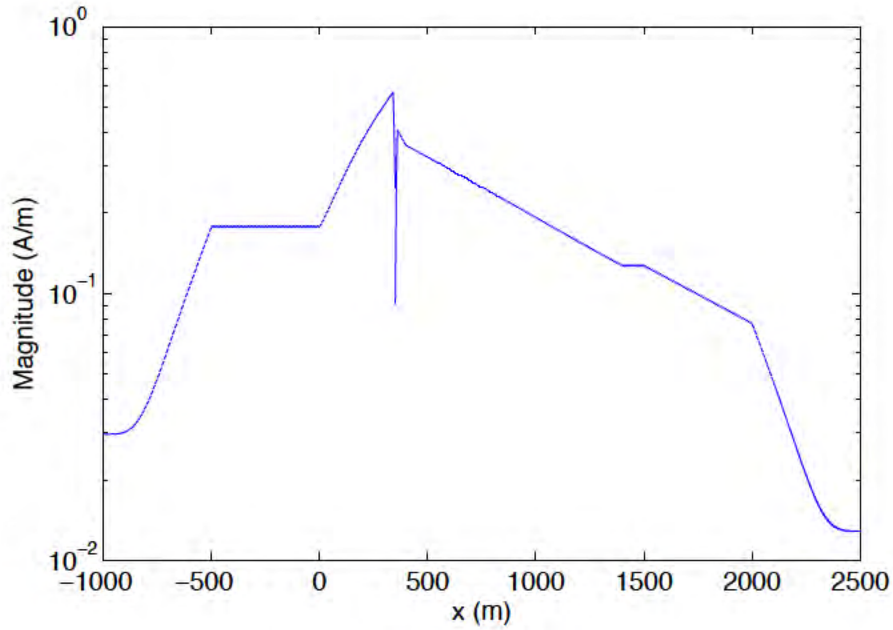

(a) Magnitude of h_y.

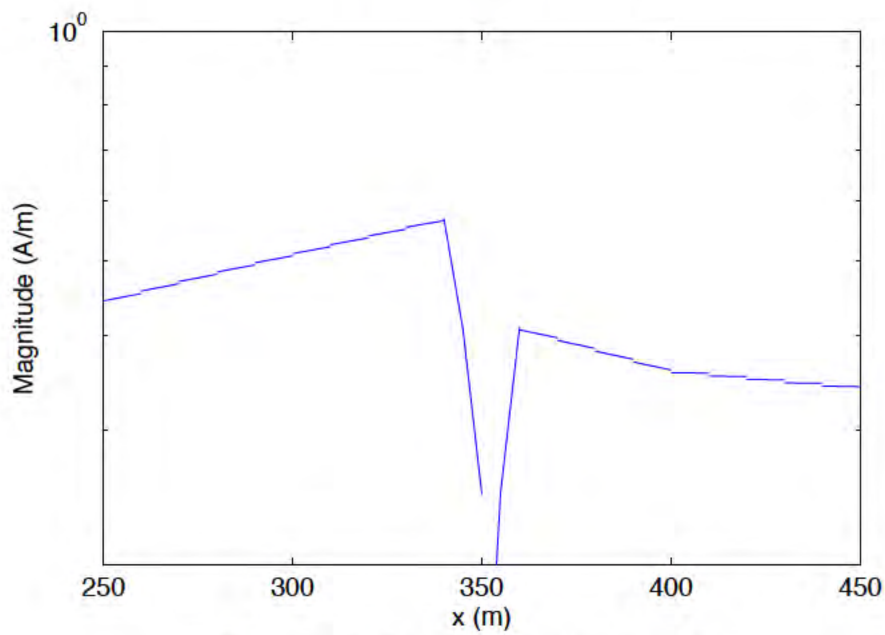

(b) Magnitude of h_y, zoomed in on source region.

FIG. 6. *Magnitude of magnetic field as a function of depth.*

5.2. Modeling in 2.5D. 2.5D modeling denotes the situation of a 3D source over a 2D earth, and is a very popular setting in geophysics. As marine geophysical data is traditionally acquired along lines, medium invariance in the direction orthogonal to the sailing line is often assumed in modeling. Due to the model invariance along one direction, the problem can be reduced from solving a 3D problem to solving a very limited number of 2D problems, thus also reducing the computational workload. These factors together make the 2.5D approximation attractive in geophysics; it allows for fast computations while still preserving the 3D nature of the source. The governing equations for this approach is given in Appendix B. We display the results in the vertical plane containing the sailing line/line of receivers. For all of the examples the source polarization is in the same plane, thus only $e_x, e_z, h_y \neq 0$. The triangular meshes were constructed using the software Triangle [31].

5.2.1. Convergence test. First we perform a convergence test. We use a homogeneous $\sigma =$ 1S/m model without any PML zones, $\epsilon = 0$F/m, $\mu = \mu_0$. The source is placed at the center of a 10000m $\times$ 10000m large model with a frequency 0.25Hz and width of 50m. The solutions obtained for different mesh sizes are compared to a solution with a significantly smaller mesh size to estimate the convergence order. We observe from Figure 7, which shows the L^2 error in the electric field against the square root of the degrees of freedom (DOFS) of the corresponding linear system, that the convergence appears to be of first order. We note that the PML zones may destroy this convergence rate, especially if the PML parameter χ is chosen large to obtain short PML zones (see Appendix A).

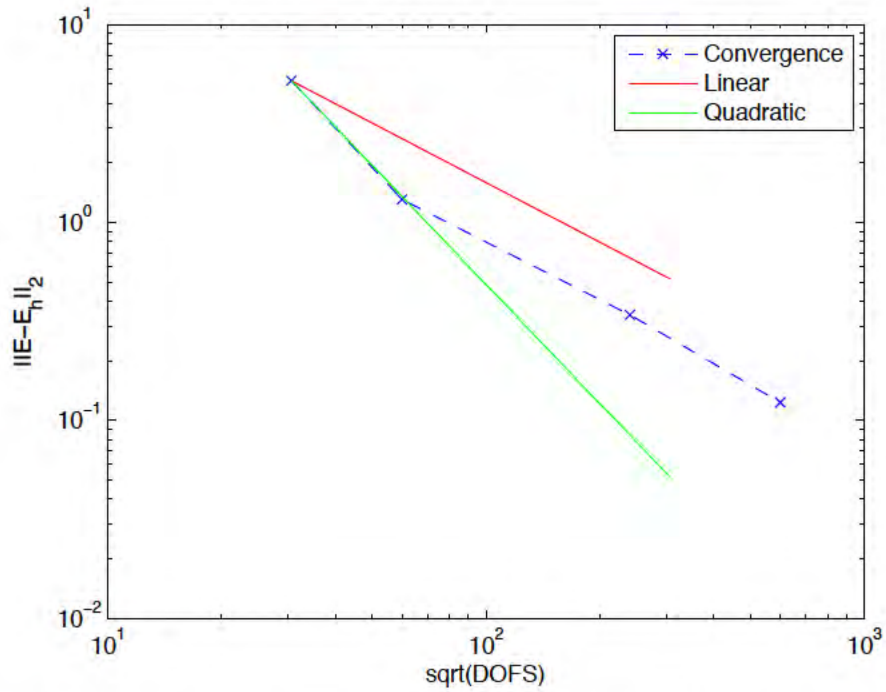

FIG. 7. *2.5D convergence test. L^2 norm of the error in the electric field against square root of degrees of freedom.*

5.2.2. Plane layer benchmark. We present here the solution in a plane layer model, for which a semi-analytical solution is known [22]. The model is shown in Figure 8, and is similar to that used by [23] except with the introduction of an air layer. The results are obtained using a source radius of $\tau = 6.25$m, 26 wavenumbers, and a frequency of 1Hz. The computational domain is $-25000\text{m} \leq x \leq 25000\text{m}$, $-50000\text{m} \leq z \leq 5000\text{m}$. The nodal distance is about 500m in the outermost region, and is reduced towards 100m and 50m in the x and z directions, respectively, in the center of the model. The mesh is further refined at material interfaces to treat these properly. The model consists of a highly resistive air layer ($\sigma = 10^{-10}$S/m), a 1000m water layer with conductivity 3.2S/m, and a subsurface conductivity of 1S/m. Within this, a 100m thick 0.01S/m layer is embedded 1000m below the seabed. The source is placed at $x = 0$m and $z = 950$m.

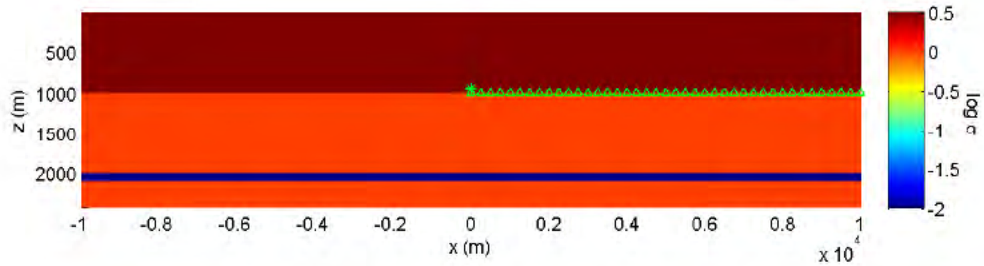

FIG. 8. *2.5D plane layer model. The green star denotes the source position and the green triangles the receiver positions.*

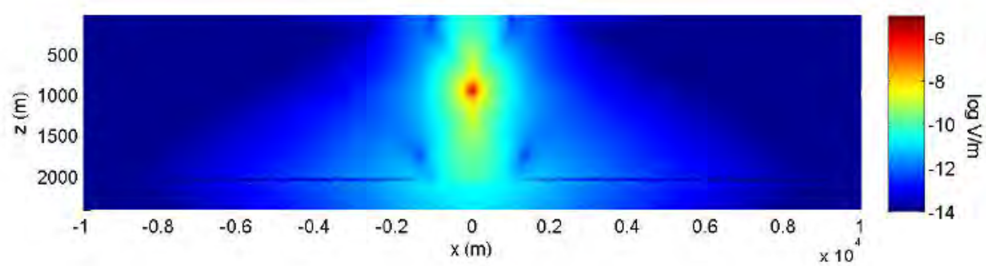

(a) e_x.

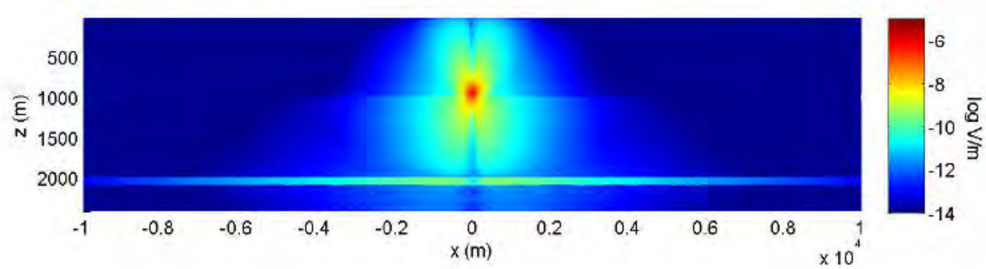

(b) e_z.

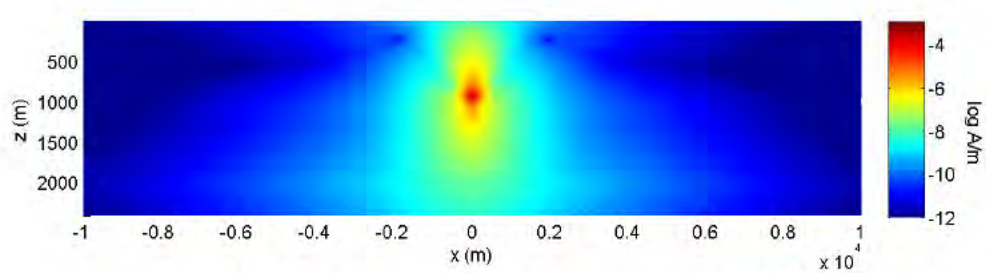

(c) h_y.

FIG. 9. *Magnitude of non-zero field components in 2.5D plane layer model.*

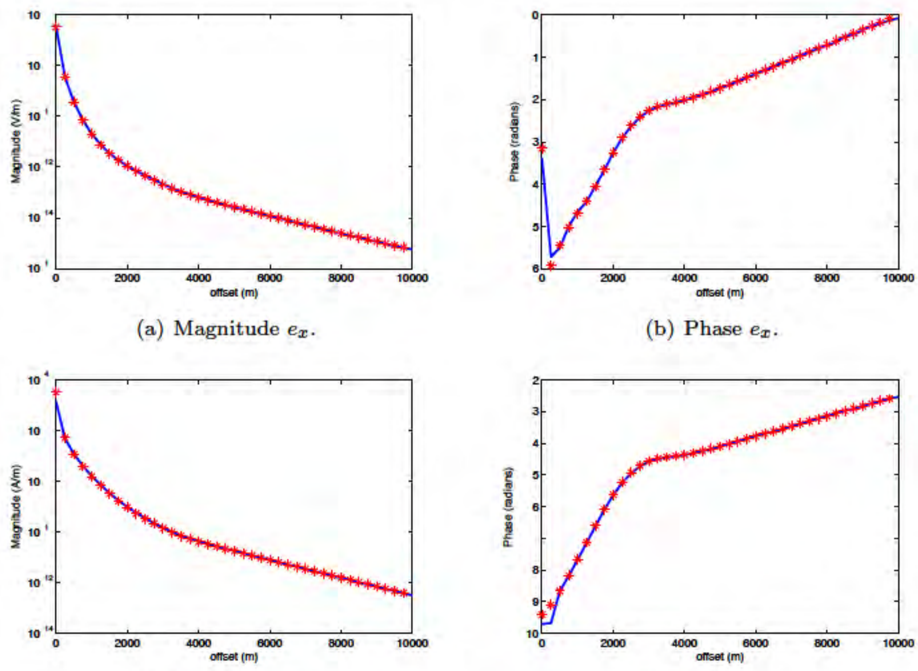

(a) Magnitude e_x. (b) Phase e_x.

(c) Magnitude h_y. (d) Phase h_y.

FIG. 10. *Magnitude and phase of mCSEM measurements along seabed.*

Figure 9 shows the non-zero field components in the model, while Figure 10 shows the magnitude and phase along the seabed for e_x and h_y, which are the usual mCSEM measurements. Figure 11 shows the real and imaginary part of the electric field normalized against the total field strength. In Figure 10 we observe a good correspondance with the semi-analytic solution, except for short horizontal offsets. This is expected due to the source approximation. The guided wave in the reservoir [20] with a dominant vertical electric field component is clearly visible from Figure 9. In Figures 11(c) and 11(d) we have zoomed in on the reservoir region, and the vertical vector field in the thin resistive layer is clear. This implies that within in a thin resistive layer we are only sensitive to the vertical conductivity, which is important to be aware of when interpreting mCSEM results. Further, the phase behaviour is clearly visible from Figures 11(a) and 11(b), where we observe the variation between large real and imaginary parts. Directly beneath the sea surface we see that the currents are perfectly horizontal, because the air acts as an almost perfect insulator.

For an even closer look at the results, consider Figures 12-14. In these figures we have zoomed in on a region around the reservoir, and we show the model with the mesh, and the amplitudes of e_x and e_z from 1D semi-analytical and 2.5D DG modeling, respectively. From Figures 13 and 14 we see the resemblance between the 2.5D DG method and the 1D semi-analytical modeling results. Inside the reservoir the electric field is almost purely vertical. Thus, e_x suffers from numerical round-off errors. However, these do not affect the end result at the receivers significantly because the vertical field is well approximated. We observe how well the DG method handles the discontinuity at the material interface. Some anomalous amplitude builds up at the interface, but the discontinuous nature of DG allows for the solution to jump back to its proper value.

This example was discretized into approximately 277 000 triangles, and used approximately 3 minutes to solve the linear system for a given wavenumber using a single 2.3GHz core.

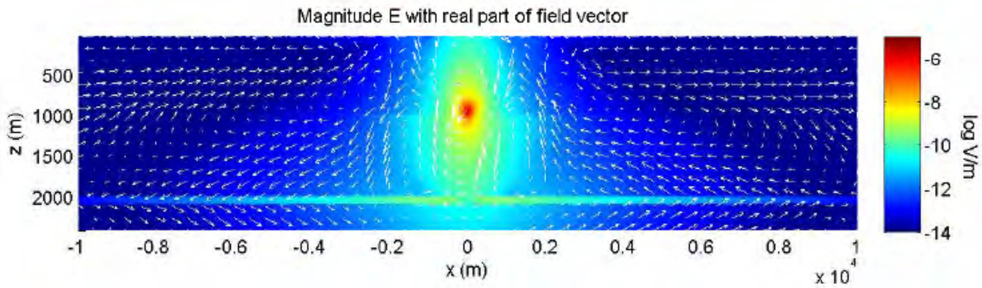

(a) Real part.

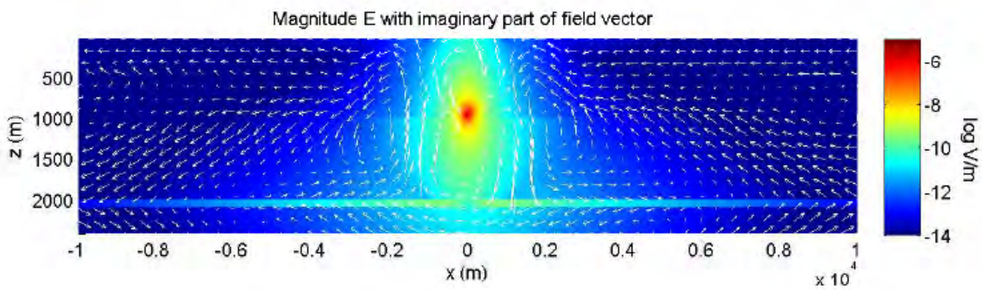

(b) Imaginary part.

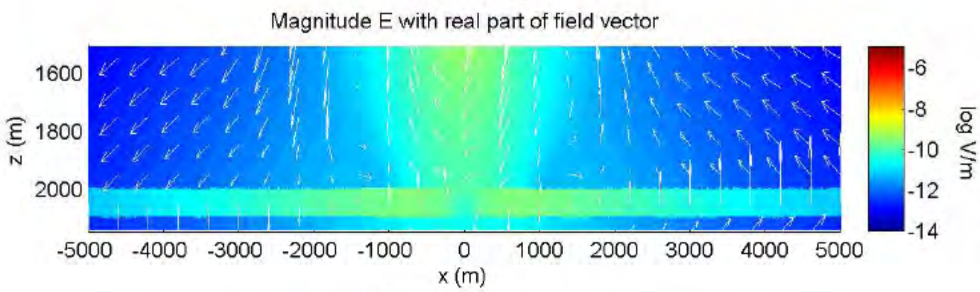

(c) Zoom in on real part.

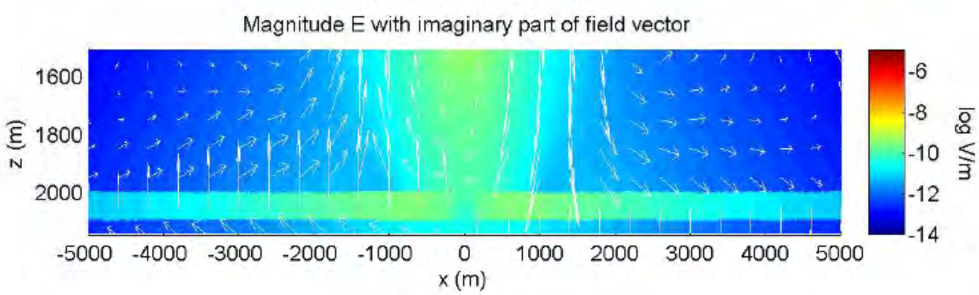

(d) Zoom in on imaginary part.

FIG. 11. *Real and imaginary part of the normalized electric field vector plotted on top of the electric field strength for the plane layer model.*

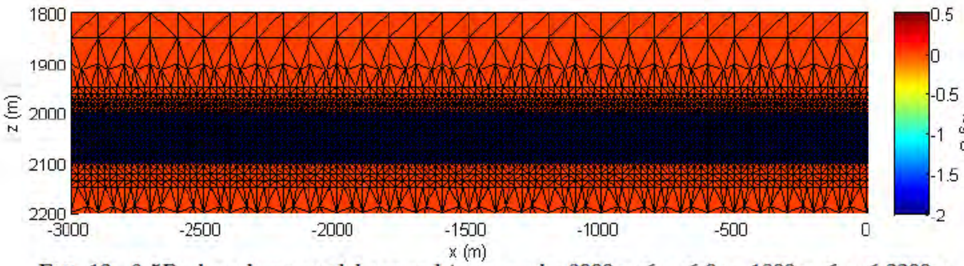

FIG. 12. *2.5D plane layer model zoomed in around $-3000m \leq x \leq 0m$, $1800m \leq z \leq 2200m$*

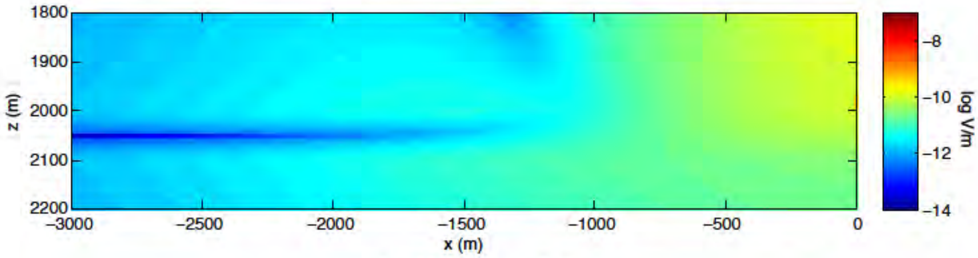

(a) 1D semi-analytical.

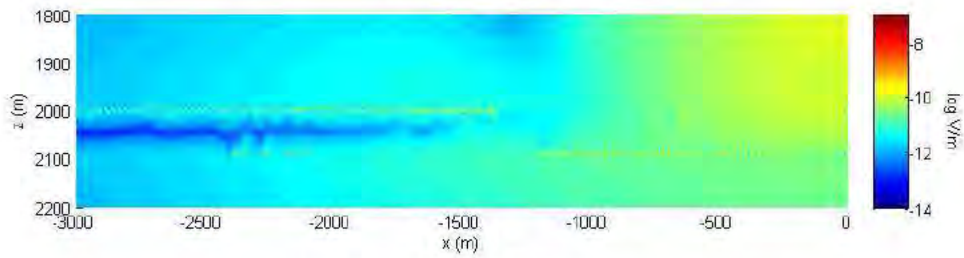

(b) 2.5D DG.

FIG. 13. *Amplitude of e_x in model shown in Figure 12*

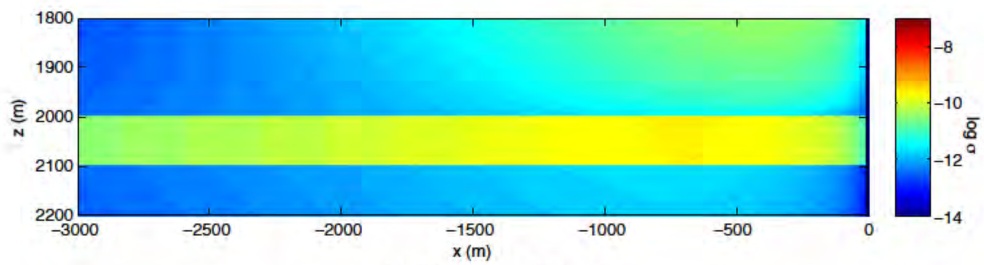

(a) 1D semi-analytical.

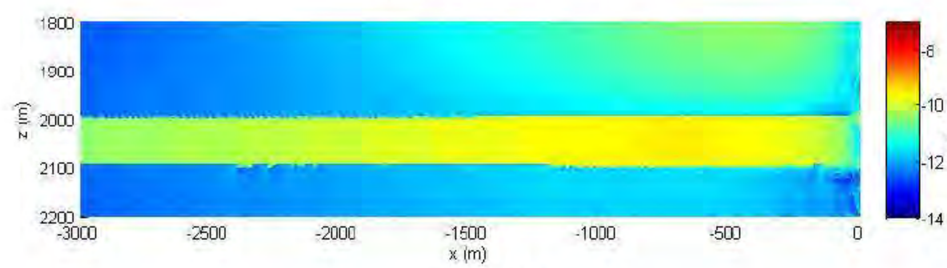

(b) 2.5D DG.

FIG. 14. *Amplitude of e_z in model shown in Figure 12*

5.2.3. Realistic model. We present here the solution in a more complex and realistic model to test the ability of the method. The model is shown in Figure 15. The results are obtained using a source radius of $\tau = 6.25$m, 26 wavenumbers and a frequency of 1.5Hz. The computational domain is $-25000\text{m} \leq x \leq 25000\text{m}$, $-50000\text{m} \leq z \leq 3000\text{m}$. The model consists of a highly resistive air layer ($\sigma = 10^{-10} S/m$), and a water layer with conductivity 3.2S/m. The subsurface consists of three layers with dipping trends, where the top layer is anisotropic. Anisotropy is a major factor in mCSEM prospecting, and the ratio between the horizontal and vertical conductivity can often reach 5. Within this a hydrocarbon reservoir with conductivity 0.02S/m is embedded. The source is placed at $x = 0$m and $z = 450$m.

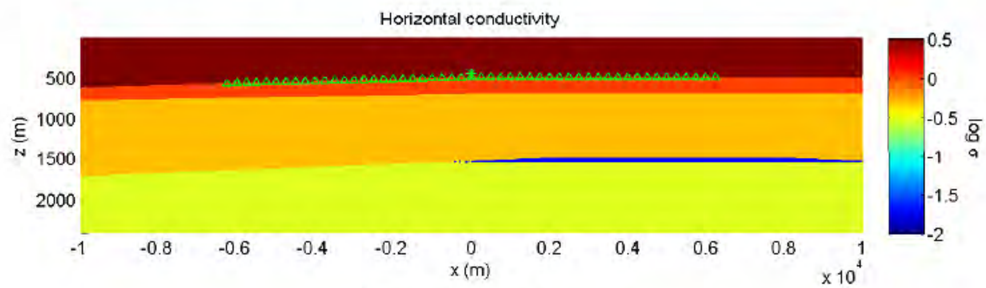

(a) Horizontal conductivity.

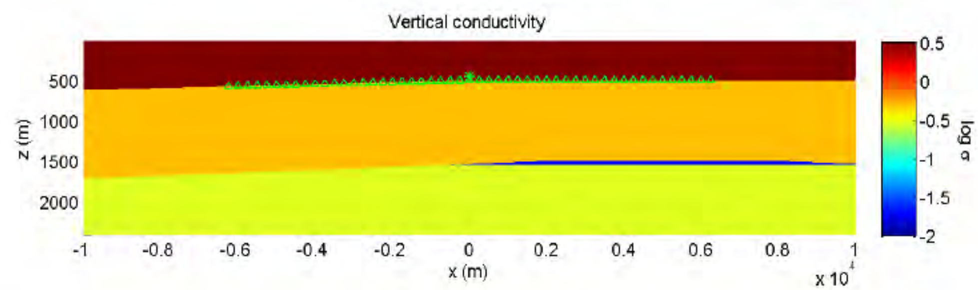

(b) Vertical conductivity.

FIG. 15. *Model used in realistic example. The green star denotes the source position and the green triangles the receiver positions.*

Figure 16 shows the field magnitudes in the model, while Figure 17 shows the magnitude and phase of the typical mCSEM measurements e_x and h_y along the seabed until the response from the air dominates. The guided wave in the reservoir with a dominant vertical electric field is again clearly visible in Figure 16. Further, the effect of the air is also clearly visible. From Figure 17, we can again observe the effect of the air, which causes the roll-over in the phase, especially for e_x. This is more prominent compared to the plane layer test due to the more shallow water column and higher frequency. For the positive offsets we compare the results with the corresponding 1D model, which confirms that the anisotropy is properly taken care of and that it models accurate results. We also note the disctinct difference of the 1D response with and without the hydrocarbon reservoir present. We observe the asymetry with respect to offest due to the lateral changes in the model. Again, the guided wave within the reservoir and the current flow are obvious from Figure 18. We also observe the discontinuity in the field at the seabed, where there is a relatively large contrast from sea water to sediments.

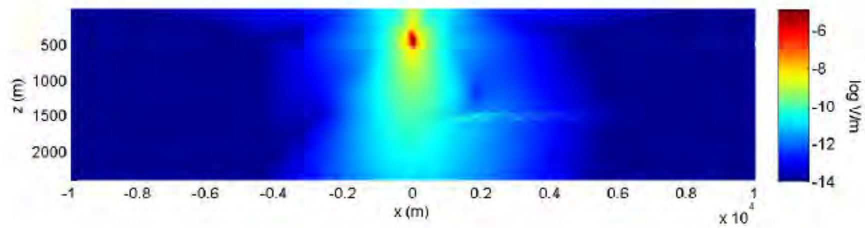

(a) e_x.

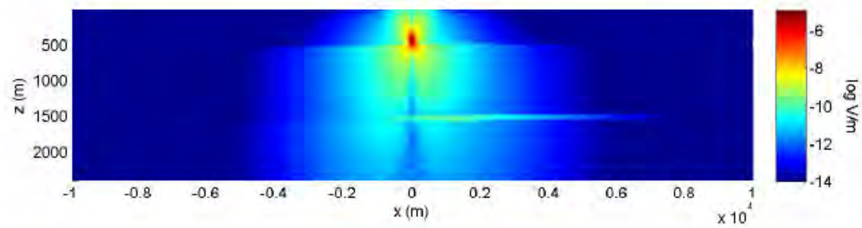

(b) e_z.

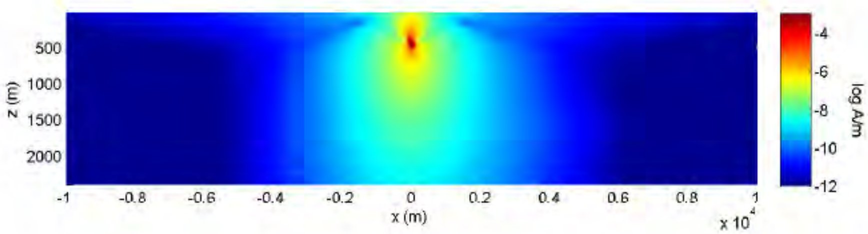

(c) h_y.

FIG. 16. *Magnitude of all fields in 2.5D realistic model.*

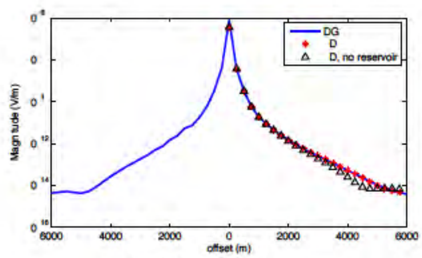

(a) Magnitude e_x.

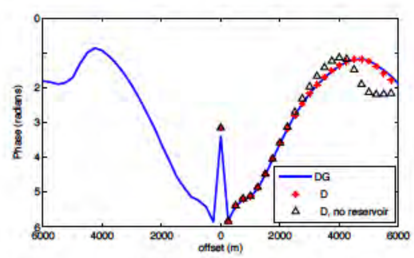

(b) Phase e_x.

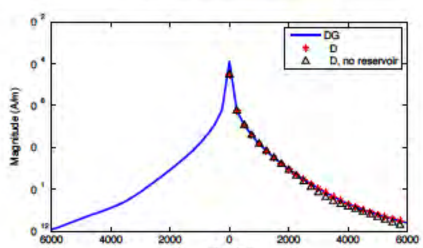

(c) Magnitude h_y.

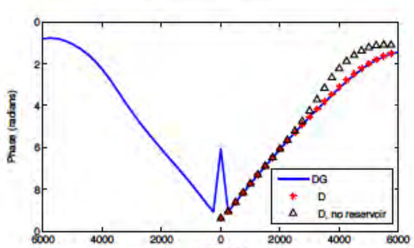

(d) Phase h_y.

FIG. 17. *Magnitude and phase of fields in 2.5D realistic model along seabed.*

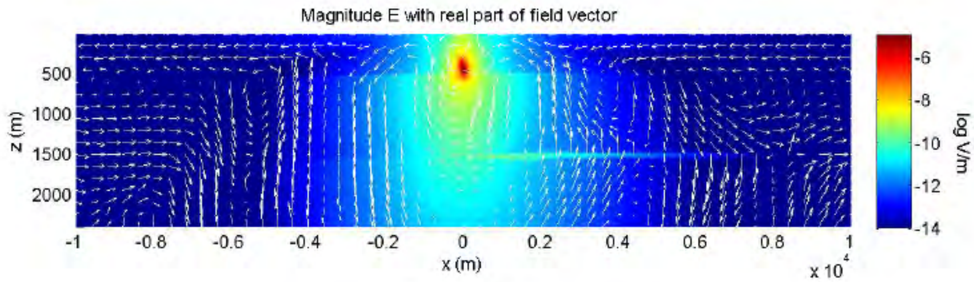

(a) Real part.

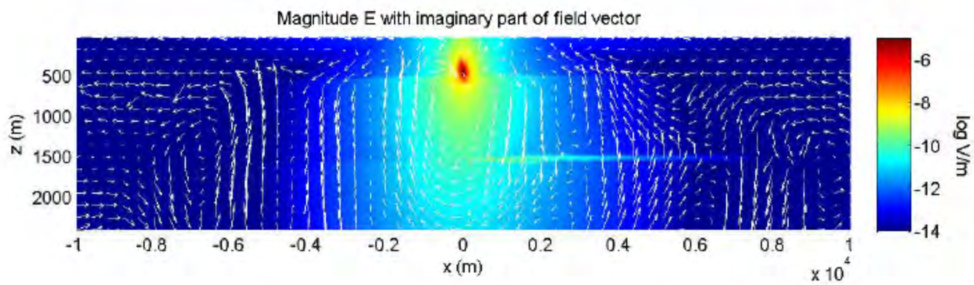

(b) Imaginary part.

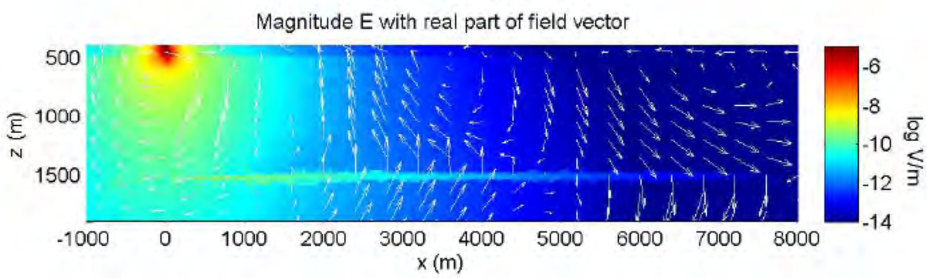

(c) Zoom in on real part.

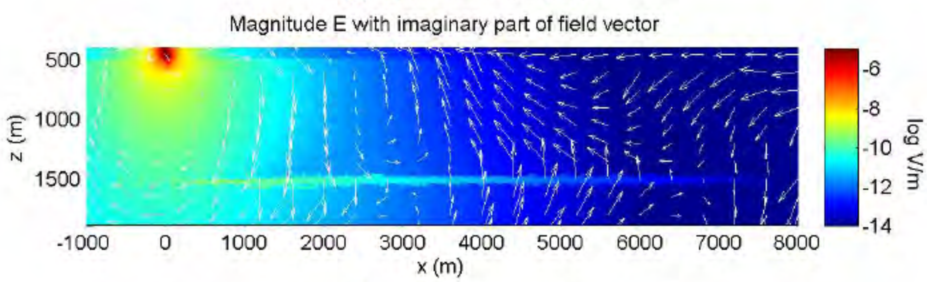

(d) Zoom in on imaginary part.

FIG. 18. *Real and imaginary part of the normalized electric field vector plotted on top of the electric field strength for the realistic model.*

5.2.4. Salt model. Finally, we present a model including a highly resistive 10^{-3}S/m salt diapir. The model is shown in Figure 19. The results are obtained using a source radius of $\tau = 6.25$m, 26 wavenumbers and a frequency of 0.75Hz. The computational domain is $-25000\text{m} \leq x \leq 25000\text{m}$, $-50000\text{m} \leq z \leq 3000\text{m}$. The model consists of a highly resistive air layer ($\sigma = 10^{-10}$S/m), and a water layer with conductivity 3.2S/m. The subsurface consists of three layers, and the salt diapir rises from below. The lowermost layer has a conductivity of 0.01S/m, and the colorscale is clipped at 0.01S/m for vizualisation. The source is placed at $x = 1000$m and $z = 800$m, above a steeply dipping part of the seabed. Figure 20 shows the field magnitudes in the model, while Figure 21 shows the magnitude and phase of the typical mCSEM measurements e_x and h_y along the seabed. From these figures, we clearly see the effect of the highly resistive salt diapir, suggesting that EM methods are suitable for imaging these. Mapping salt structures using mCSEM is an extreme case due to the very large resistivities, and the fact that salt structures can be large in size. This makes the effect on mCSEM data very prominent. The approximately flat phases in Figure 21 indicate a very high propagation speed, consistent with the high salt resistivity. From Figure 22 we see how the currents, given by $\tilde{\sigma}\mathbf{e}$, travel around the resistive diapir. Figures 22(c) and 22(d) show the vector fields zoomed in around the top of the salt and seabed, and illustrates how the different interfaces affect the electric field behaviour. The fields are strongly affected by the resistive salt.

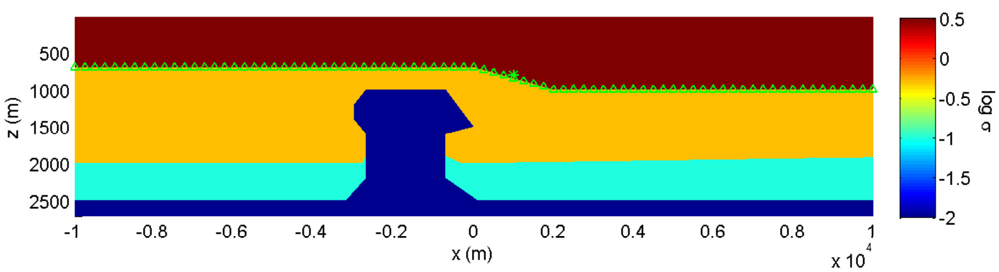

FIG. 19. *Model used in salt example. The green star denotes the source position and the green triangles the receiver positions.*

6. Discussion. We have demonstrated the properties of frequency domain DG modeling of mCSEM data. The DG framework is flexible with respect to mesh (h) and polynomial order (p) refinement, and is able to handle large contrasts in properties at material interfaces due to its discontinuous nature. Both are important properties for electromagnetic methods in geophysics, although only first order basis functions were discussed here. The accuracy of the method is estimated to increase linearly as a function of decreasing mesh size. However, the corresponding linear system of equations is often very stiff due to the unstructured nature of the mesh and the large parameter variations. Thus, one needs to be careful when solving the system. We demonstrate the method on several examples, showing the validation and capability of the implemetation, and illustrating the physics of the mCSEM problem. For the 2.5D setting, the computational time is not heavily dependent on the number of wavenumbers chosen, as each of them is treated in parallell.

7. Acknowledgements. The authors would like to acknowledge the help from Dr. Per-Olof Persson of the University of California at Berkeley for many helpful discussions, and Dr. Peijun Li of Purdue University for his help with the PML formulation. Torgeir Wiik acknowledges Statoil ASA for sponsoring his Ph.D. project. Bjørn Ursin has received financial support from VISTA and from the Norwegian Research Council through the ROSE project at NTNU. The research was supported in part by the members of GMIG at Purdue University, BGP, ExxonMobil, PGS, Statoil and Total.

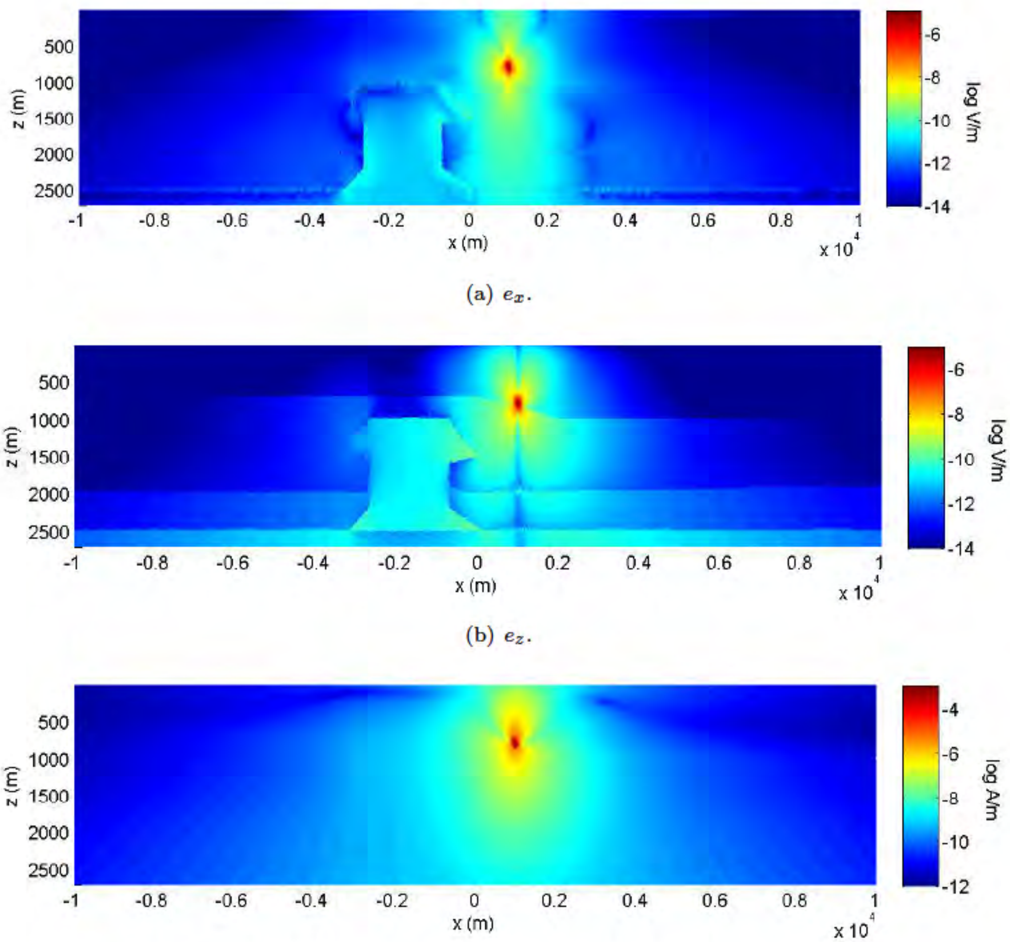

(a) e_x.

(b) e_z.

(c) h_y.

FIG. 20. *Magnitude of all fields in 2.5D salt model.*

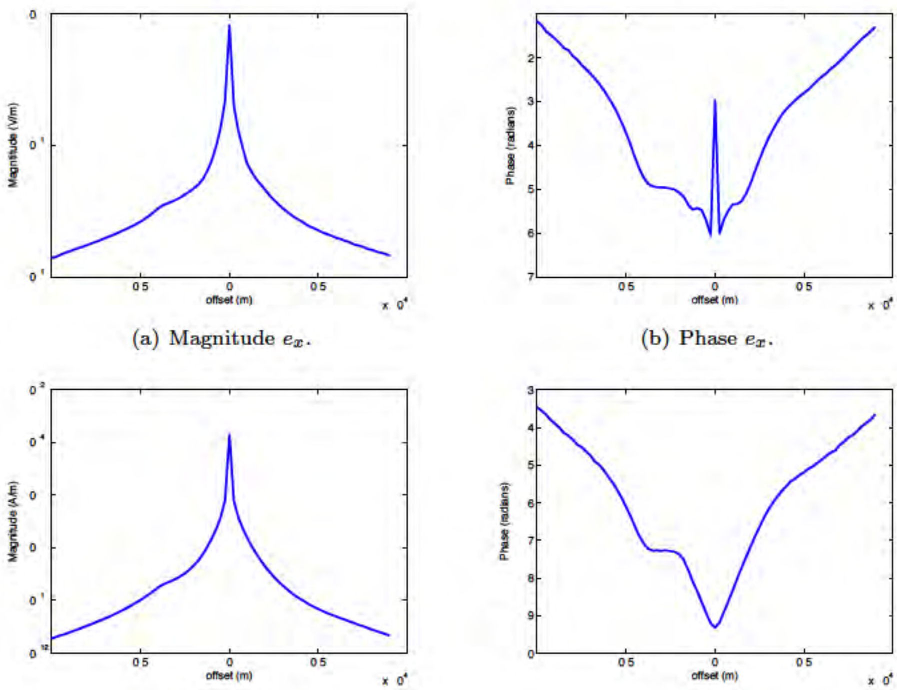

(a) Magnitude e_x.

(b) Phase e_x.

(c) Magnitude h_y.

(d) Phase h_y.

FIG. 21. *Magnitude and phase of fields in 2.5D salt model along seabed.*

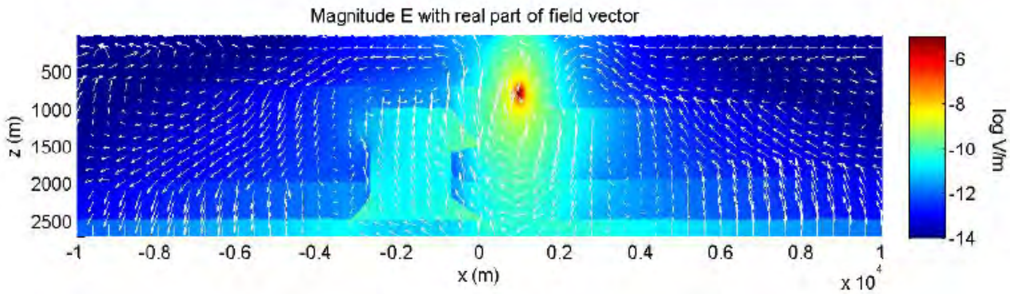

(a) Real part.

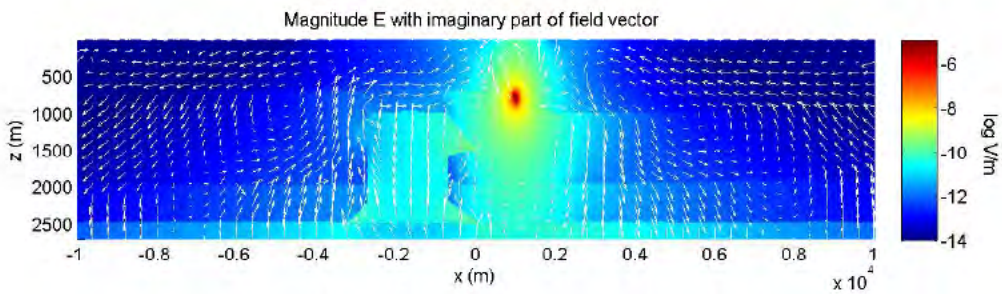

(b) Imaginary part.

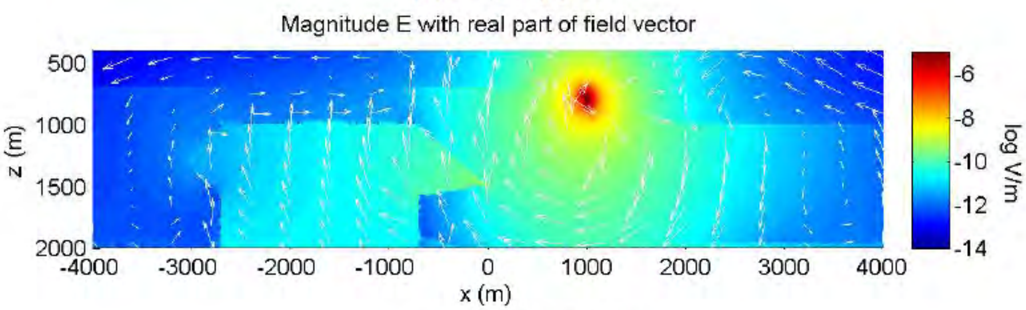

(c) Zoom in on real part.

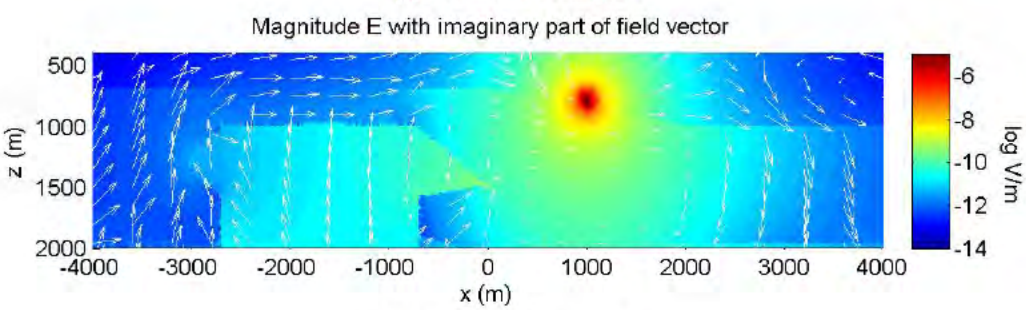

(d) Zoom in on imaginary part.

FIG. 22. *Real and imaginary part of the normalized electric field vector plotted on top of the electric field strength for the salt model.*

Appendix A. PML boundaries. To simulate the radiation condition given in equation 2.3 with equations 2.1 and 2.2 one would need a large domain computational Ω_h. This again would increase the computational cost. To avoid this, a strategy using *Perfectly Matched Layers* (PML) was implemented. This involves padding the domain Ω with an absorbing medium to ensure that the fields are attenuated fast as they approach $\partial\Omega$, as indicated in Figure 2. However, the introduction of such a layer is not trivial. If it is done carelessly, reflections from the boundary between the normal domain and the PML will be encountered, and these will potentially pollute the solution. To avoid these reflections from the boundary the PML is designed in such a way that the fields are attenuated within this zone, but it has no contrast in impedances compared to the actual domain of interest, and thus does not cause any reflections. This attentuation emulates the radiation condition, and allows for a smaller computational domain to be chosen. Several approaches are possible, for instance the variable splitting presented by Berenger [5], and anisotropic matching [29], but we choose the complex coordinate stretching, also known as complex scaling in analysis, introduced in [7].

To this end we follow [7], and introduce the complex coordinates

$$\begin{aligned} \tilde{x} &= \int_0^x s_x\left(x'\right) \mathrm{d}x', \\ \tilde{y} &= \int_0^y s_y\left(y'\right) \mathrm{d}y', \\ \tilde{z} &= \int_0^z s_z\left(z'\right) \mathrm{d}z', \end{aligned} \tag{A.1}$$

where $s_j\left(\tau\right) = \zeta_j^1\left(\tau\right) + \mathrm{i}\zeta_j^2\left(\tau\right)$ is a continuous function satisfying

$$\begin{aligned} \zeta_j^1 &= 1, \quad \zeta_j^2 = 0 \quad \text{outside the PML zone,} \\ \zeta_j^1 &\geq 1, \quad \zeta_j^2 > 0 \quad \text{inside the PML zone,} \end{aligned}$$

such that the coordinates coincides with the ordinary cartesian coordinates outside the PML zone. The gradient in the stretched coordinate system becomes

$$\tilde{\nabla} = \left[\frac{\partial}{\partial\tilde{x}}, \frac{\partial}{\partial\tilde{y}}, \frac{\partial}{\partial\tilde{z}}\right],$$

where $\frac{\partial}{\partial\tilde{x}} = \frac{1}{s_x}\frac{\partial}{\partial x}$. Maxwell's equations then become

$$\tilde{\nabla} \times \mathbf{e} = \mathrm{i}\omega\mu_0\mathbf{h}, \tag{A.2}$$

$$\tilde{\nabla} \times \mathbf{h} = \tilde{\sigma}\mathbf{e} + \mathbf{j}^s, \tag{A.3}$$

$$\tilde{\nabla} \cdot \left(\epsilon\mathbf{e}\right) = 0, \tag{A.4}$$

$$\tilde{\nabla} \cdot \left(\mu_0\mathbf{h}\right) = 0, \tag{A.5}$$

which looks as usual, except the coordinates may be complex. In practice $s_j\left(\tau\right)$ is taken as a power function, that is

$$s_j\left(\tau\right) = 1 + \chi\left(\frac{d\left(\tau\right)}{\delta}\right)^m, \quad m \geq 1,$$

where $d\left(\tau\right)$ is the distance in the j-direction to the boundary between the ordinary zone and the PML zone, and δ is the thickness of the PML zone. It can be verified that increasing the thickness δ, or increasing $\mathrm{Re}\left(\chi\right)$ and $\mathrm{Im}\left(\chi\right)$, will reduce the PML approximation error.

Appendix B. 2.5D frequency domain formulation. In this appendix we consider the 2.5D situation described in the section concerning numerical results. We proceed by considering a sailing line in the x-direction, making the y-direction model invariant. We use the Fourier convention given by the forward transform

$$\hat{F}(k_y) = \int_{\mathbb{R}} F(y)\, e^{\mathrm{i}k_y y} \mathrm{d}y,$$

and apply it to equations 2.1 and 2.2. This gives the following 2.5D frequency domain system written componentwise:

$$\begin{aligned}
-\mathrm{i}k_y h_z - \frac{\partial}{\partial z} h_y &= \tilde{\sigma} e_x + j_x,\\
\frac{\partial}{\partial z} h_x - \frac{\partial}{\partial x} h_z &= \tilde{\sigma} e_y + j_y,\\
\frac{\partial}{\partial x} h_y + \mathrm{i}k_y h_x &= \tilde{\sigma} e_z + j_z,\\
-\mathrm{i}k_y e_z - \frac{\partial}{\partial z} e_y &= \mathrm{i}\omega\mu_0 h_x,\\
\frac{\partial}{\partial z} e_x - \frac{\partial}{\partial x} e_z &= \mathrm{i}\omega\mu_0 h_y,\\
\frac{\partial}{\partial x} e_y + \mathrm{i}k_y e_x &= \mathrm{i}\omega\mu_0 h_z,
\end{aligned} \tag{B.1}$$

where we have omitted to denote the hat for Fourier transformed quantities. These PDEs are in 2D space for each k_y. Thus, the corresponding basis functions depend only on x and z, while the expansion coefficients will depend on k_y.

Following the procedure from earlier gives the following weak formulation for a given wavenumber k_y:

Find $\mathbf{e}^h, \mathbf{h}^h \in X$ *such that the following equations hold* $\forall v \in X$*, for each* $K \in \tau_h$*.*

$$\begin{aligned}
-\int_{\partial K} h_y^h v_x n_z \mathrm{d}S - \mathrm{i}k_y \left(h_z^h, v_x\right)_K + \left(h_y^h, \frac{\partial}{\partial z} v_x\right)_K &= \left(\tilde{\sigma} e_x^h, v_x\right)_K + \left(j_x, v_x\right)_K,\\
\int_{\partial K} h_x^h v_y n_z \mathrm{d}S - \int_{\partial K} h_z^h v_y n_x \mathrm{d}S - \left(h_x^h, \frac{\partial}{\partial z} v_y\right)_K &= \left(\tilde{\sigma} e_y^h, v_y\right)_K + \left(j_y, v_y\right)_K,\\
\int_{\partial K} h_y^h v_z n_x \mathrm{d}S + \mathrm{i}k_y \left(h_x^h, v_z\right)_K - \left(h_y^h, \frac{\partial}{\partial x} v_z\right)_K &= \left(\tilde{\sigma} e_z^h, v_z\right)_K + \left(j_z, v_z\right)_K,\\
-\int_{\partial K} e_y^h v_x n_z \mathrm{d}S - \mathrm{i}k_y \left(e_z^h, v_x\right)_K + \left(e_y^h, \frac{\partial}{\partial z} v_x\right)_K &= \left(\mathrm{i}\omega\mu_0 h_x^h, v_x\right)_K,\\
\int_{\partial K} e_x^h v_y n_z \mathrm{d}S - \int_{\partial K} e_z^h v_y n_x \mathrm{d}S - \left(e_x^h, \frac{\partial}{\partial z} v_y\right)_K &= \left(\mathrm{i}\omega\mu_0 h_y^h, v_y\right)_K,\\
\int_{\partial K} e_y^h v_z n_x \mathrm{d}S + \mathrm{i}k_y \left(e_x^h, v_z\right)_K - \left(e_y^h, \frac{\partial}{\partial x} v_z\right)_K &= \left(\mathrm{i}\omega\mu_0 h_z^h, v_z\right)_K.
\end{aligned} \tag{B.2}$$

Here $v_i, i = x, y, z$ denotes the components of the basis function v.

Solving the corresponding linear system of equations will give the fields in the spatial wavenumber domain. To obtain the fields in the spatial domain we perform an inverse Fourier transform using cubic spline interpolation between the wavenumbers and a Gaussian quadrature. [24] suggests an upper bound for selecting the wavenumbers, and that they should be chosen on a logarithmic scale.

REFERENCES

[1] D. Arnold. An interior penalty finite-element method with discontinuous elements. *SIAM Journal on Numerical Analysis*, 19:742–760, 1982.

[2] I. Babuška. The finite element method with penalty. *Math. Comp.*, 27:221–228, 1973.

[3] I. Babuška and M. Zlámal. Nonconforming elements in th finite element method with penalty. *SIAM Journal on Numerical Analysis*, 10:863–875, 1973.

[4] G. Baker. Finite element methods for elliptic equations using non-conforming elements. *Math. Comp.*, 31:45–59, 1977.

[5] J. Berenger. Three-dimensional perfectly matched layer for the absorption of electromagnetic waves. *Journal of Computational Physics*, 127:363–379, 1996.

[6] A. L. Buffa and I. Perugia. Discontinuous Galerkin approximation of the Maxwell eigenproblem. *SIAM Journal on Numerical Analysis*, 44:2198–2226, 2006.

[7] W. C. Chew, J. M. Jin, and E. Michielssen. Complex coordinate stretching as a generalized absorbing boundary condition. *Microwave and Optical Technology Letters*, 15:363–369, 1997.

[8] B. Cockburn, G Karniadakis, and C.-W. Shu. The development of discontinuous Galerkin methods. In B. Cockburn, G. Karniadakis, and C.-W. Shu, editors, *Discontinuous Galerkin Methods. Theory, Computation and Applications*, Lecture notes in Computational Science and Engineering, pages pp.3–50. Springer Verlag, 2000.

[9] B. Cockburn, F. Li, and C.-W. Shu. Locally divergence-free discontinuous Galerkin methods for the Maxwell equations. *Journal of Computational Physics*, 194:588–610, 2004.

[10] B. Cockburn and C. Shu. The local discontinuous Galerkin method for time-dependent convection-diffusion systems. *SIAM Journal on Numerical Analysis*, 35:2440–2463, 1998.

[11] N.V. da Silva, J. V. Morgan, L. MacGregor, and M. Warner. A finite element multifrontal method for 3D CSEM modeling in the frequency domain. *Geophysics*, 77:E101–E115, 2012.

[12] V. Dolean, H. Fol, S. Lanteri, and R. Perrussel. Solution of the time-harmonic Maxwell equations using discontinuous Galerkin methods. *Journal of Computational and Applied Mathematics*, 218:435–445, 2008.

[13] J. Douglas Jr and T. Dupont. Interior penalty procedures for elliptic and parabolic Galerkin methods. In *Lecture notes in physics*. Springer, Berlin, 1976.

[14] T Eidesmo, S Ellingsrud, L M MacGregor, S Constable, M C Sinha, S Johansen, F N Kong, and H Westerdal. Sea bed logging (sbl), a new method for remote and direct identification of hydrocarbon filled layers in deepwater areas. *First Break*, 20:144–152, 2002.

[15] A. Ern and J.-L. Guermond. Discontinuous Galerkin methods for Friedrichs' systems. Part I. General theory. *SIAM Journal on Numerical Analysis*, 44:753–778, 2006.

[16] J. S. Hesthaven and T. Warburton. *Nodal Discontinuous Galerkin Methods. Algorithms, Analysis, and Applications*. Springer New York, 2008.

[17] P. Lesaint and P.-A. Raviart. On a finite element method for solving the neutron transport equation. In *Mathematical Aspects of Finite Elements in Partial Differential Equations*, number 33, pages pp.89–123. Academic Press, New York, 1974.

[18] Y. Li and K. Key. 2D marine controlled-source electromagnetic modeling: Part 1 - An adaptive finite-element algorithm. *Geophysics*, 72:WA51–WA62, 2007.

[19] Y. Liu, Q. Hu, and D. Yu. A non-overlapping domain decomposition for low-frequency time-harmonic Maxwell's equations in unbounded domains. *Advances in Computational Mathematics*, 28:355–382, 2008.

[20] L. Løseth. Marine CSEM signal propagation in TIV media. *SEG Technical Program Expanded Abstracts*, 26:638–642, 2007.

[21] L. O. Løseth. *Modelling of controlled source electromagnetic data*. PhD thesis, Norwegian University of Science and Technology, 2007.

[22] L. O. Løseth and B. Ursin. Electromagnetic fields in planarly layered anisotropic media. *Geophysical Journal International*, 170:44–80, 2007.

[23] F. A. Maaø. Fast finite-difference time-domain modeling for marine-subsurface electromagnetic problems. *Geophysics*, 72:A19–A23, 2007.

[24] Y. Mitsuhata. 2-D electromagnetic modeling by finite-element method with a dipole source and topography. *Geophysics*, 65:465–475, 2000.

[25] M. N. Nabighian, editor. *Electromagnetic Methods in Applied Geophysics*. Society of Exploration Geophysicists, Oklahoma, 1987.

[26] J.-C. Nédélec. Mixed finite elements in $\mathbb{R}^3$. *Numerische Mathematik*, 35:315–341, 1980.

[27] S. Piperno, M. Remaki, and L. Fezoui. A nondiffusive finite volume scheme for the three-dimensional Maxwell's equations on unstructured meshes. *SIAM Journal on Numerical Analysis*, 39:2089–2108, 2002.

[28] W. Reed and T. Hill. Triangular mesh methods for the neutron transport equation. Technical Report LA-UR-73-479, Los Alamos Scientific Laboratory, Los Alamos, 1973.

[29] Z. S. Sacks, D. M. Kingsland, R. Lee, and J. Lee. A perfectly matched anisotropic absorber for use as an absorbing boundary condition. *IEEE Transactions on Antennas and Propagation*, 43:1460–1463, 1995.

[30] A. Schneebeli. *Interior penalty discontinuous Galerkin methods for electromagnetic and acoustic wave equations*. PhD thesis, Universität Basel, 2006.

[31] Jonathan Richard Shewchuk. Triangle: Engineering a 2D quality mesh generator and Delaunay triangulator.

In Ming C. Lin and Dinesh Manocha, editors, *Applied Computational Geometry: Towards Geometric Engineering*, volume 1148 of *Lecture Notes in Computer Science*, pages 203–222. Springer-Verlag, may 1996. From the First ACM Workshop on Applied Computational Geometry.

[32] C. H. Stoyer and R. J. Greenfield. Numerical solutions of the response of a two-dimensional earth to an oscillating magnetic dipole source. *Geophysics*, 41:519–530, 1976.

[33] J. A. Stratton. *Electromagnetic Theory.* McGraw-Hill, New York, 1941.

[34] A. H. Stroud. *Approximate calculation of multiple integrals.* Prentice-Hall, 1971.

[35] M. Wheeler. An elliptic collocation-finite element method with interior penalties. *SIAM Journal on Numerical Analysis*, 15:152–161, 1978.